remote sensing

MDPI

Article

Emerging Pattern of Wind Change over the Eurasian Marginal Seas Revealed by Three Decades of Satellite Ocean-Surface Wind Observations

Lisan Yu

Department of Physical Oceanography, Woods Hole Oceanographic Institution, Woods Hole, MA 02543, USA; lyu@whoi.edu; Tel.: +1-508-289-2504

Abstract: This study provides the first full characterization of decadal changes of surface winds over 10 marginal seas along the Eurasian continent using satellite wind observations. During the three decades (1988–2018), surface warming has occurred in all seas at a rate more pronounced in the South European marginal seas (0.4–0.6 °C per decade) than in the monsoon-influenced North Indian and East Asian marginal seas (0.1–0.2 °C per decade). However, surface winds have not strengthened everywhere. On a basin average, winds have increased over the marginal seas in the subtropical/mid-latitudes, with the rate of increase ranging from 11 to 24 cms^{-1} per decade. These upward trends reflect primarily the accelerated changes in the 1990s and have largely flattened since 2000. Winds have slightly weakened or remained little changed over the marginal seas in the tropical monsoonal region. Winds over the Red Sea and the Persian Gulf underwent an abrupt shift in the late 1990s that resulted in an elevation of local wind speeds. The varying relationships between wind and SST changes suggest that different marginal seas have responded differently to environmental warming and further studies are needed to gain an improved understanding of climate change on a regional scale.

Keywords: satellite ocean-surface winds; regional warming; decadal trends; marginal seas; the Arabian Sea; the Bay of Bengal; the Mediterranean Sea; the Red Sea; the Black Sea; the Caspian Sea; the East and South China Seas; the Sea of Japan

Citation: Yu, L. Emerging Pattern of Wind Change over the Eurasian Marginal Seas Revealed by Three Decades of Satellite Ocean-Surface Wind Observations. *Remote Sens.* **2021**, *13*, 1707. https://doi.org/10.3390/rs13091707

Academic Editors: Peter Minnett and Vladimir N. Kudryavtsev

Received: 5 April 2021
Accepted: 26 April 2021
Published: 28 April 2021

1. Introduction

Ocean surface winds are an Essential Climate Variable (ECV) identified by the Global Climate Observing System (GCOS). They play an important role in many oceanic and atmospheric processes, such as generating marine waves, driving ocean general circulation, and modulating air-sea heat, moisture, and gas fluxes. Since July 1987, the global ocean surface wind fields have been remotely sensed by two types of sensors: radar scatterometers that retrieve wind direction and speed, and passive microwave radiometers that retrieve wind speed only. The radiometric observations of wind speed have been continuous throughout the period, thanks to the uninterrupted sequence of the Defense Meteorological Satellite Program (DMSP) that carries out the Special Sensor Microwave/Imager (SSM/I) series and the follow-on Special Sensor Microwave Imager Sounder (SSMIS) series [1–3]. SSM/I is a successful instrument, and its design has become standard for passive microwave imagers, including the TRMM Microwave Imager (TMI) aboard the joint US-Japan TRMM satellite in 1997, the Advanced Microwave Scanning Radiometer-Earth Observing System (AMSR-E) instrument aboard the NASA's Earth Observing System Aqua Satellite (2002–2011), and AMSR-2 on the first satellite of the "Global Change Observation Mission" (GCOM-W1) launched by the Japan Aerospace Exploration Agency (JAXA) (2012–present). When all are combined, the data records of microwave radiometers have constituted more than 30 years of reliable and valuable measurements of ocean surface wind speed.

The global mean surface temperatures in the past 30 years have been rising at a rate unprecedented in recent geological history (Intergovernmental Panel on Climate Change (IPCC) 2007). Coinciding with the rising temperatures, the average ocean-surface wind speeds have increased [4] at an estimated rate of 0.8 cms^{-1} (1.2%) per decade during the satellite era [5,6]. The strengthened wind speeds have contributed to an increase in ocean evaporation [7], which has, in turn, intensified the global water cycle [8]. The strengthened wind speeds have also been linked to the increase of significant wave heights and extreme wave events [4,9]. Nonetheless, wind speeds alone are far from sufficient to characterize the dynamic extent of the changing global near-surface wind forcing. Changes in wind direction, even if small, cause changes in surface vorticity and divergence fields [10]. These changes drive the response of the wind-driven ocean circulation, generating spatially non-uniform patterns in sea-level rise [11] and modulating the ocean's capacity of transporting heat and salt [12–14].

The vector wind data records produced by scatterometer missions are not seamlessly connected to each other. The record lengths vary considerably with the mission, with some lasting for a few months and others staying on as long as approximately 10 years [15]. The two long-lived scatterometer missions are the NASA SeaWinds on the QuikSCAT mission (1999–2009) [16] and the Advanced Scatterometer (ASCAT) on the EUMETSAT satellite series Metop-A, -B, and -C (2006–present) [17]. The missions with a shorter span of time are the NASA Scatterometer (NSCAT) aboard the Japanese National Space Development Agency (NASDA) Advanced Earth Observing Satellite I (ADEOS–I) (nine months, 1996–1997) [18], the NASA SeaWinds-2 on NASDA ADEOS-II (10 months, 2002–2003) [19,20], the OceanSat–2 Scatterometer (OSCAT; 2009–2014) and its follow-on mission Scatterometer Satellite-1 (SCATSat-1; 2016–present) launched by the Indian Space Research Organization (ISRO) [21,22]. There were also scatterometers onboard the European Space Agency's (ESA) Earth Remote Sensing satellites, namely, ERS1 in 1991 and ERS2 in 1995.

Optimizing the use of available satellite wind retrievals is highly needed for establishing a global perspective of wind change during the recent decades of climate significance. Efforts have been made by several groups to construct vector wind time series from merging scatterometers and/or passive microwave radiometers [23–28]. This study is to use a satellite wind data record from the High-Resolution component of the Objective Analyzed air-sea Flux project (hereafter OAFlux-HR) at the Woods Hole Oceanographic Institution (WHOI) [5,29]. The OAFlux-HR vector wind analysis resulted from synthesizing 17 sensors that include 11 passive microwave radiometers and 5 scatterometers and is available on a daily 0.25° spatial resolution from 1988 onward. Strategy and methodology that address technical aspects of the development have been previously reported [25,26,30]. The latest efforts have been placed on validation and evaluation to enhance the consistency and accuracy of the time series in both the open ocean and the marginal seas.

Winds over the marginal seas warrant special attention. The marginal seas are partially enclosed bodies of water along continental margins, and they are often adjacent to or widely open to the open ocean at the surface (Wikipedia.org, accessed on 5 April 2021). In the era of global warming, the marginal seas respond more rapidly to the evolving climate changes than the open ocean owing to their small sizes and the small volume-to-surface-area ratio [31–33]. Marbà et al. [34] reported that the Mediterranean Sea is warming at two to three times the rate of the global ocean [35] and experiences an increase in the occurrence of heat extremes by 200–500% [36]. Alawad et al. [37] identified an increasing trend of sea surface temperature (SST) at about 0.4 °C per decade in the northern Red Sea that began around the mid-1990s. The warming of the Red Sea has raised the potential for damaging effects on society, the environment, and the overall ecosystem in the region [38]. Rostov et al. [33] showed that the marginal seas of East Asia, e.g., the Okhotsk Sea, the Japan Sea, and the Yellow and East China Seas, have also warmed rapidly in recent decades. Surface winds respond to the changes of SST [39,40]. However, despite the numerous

findings of accelerated warming in the enclosed and semi-enclosed coastal seas, there have been limited studies on the wind changes during the concurrent period.

The objective of this study is to identify and characterize the decadal changes of surface winds over 10 Eurasian marginal seas using the OAFlux-HR vector wind time series. The 10 marginal seas are the Mediterranean Sea, the Black Sea, the Caspian Sea, the Red Sea, the Persian Gulf, the Arabian Sea, the Bay of Bengal, the East, and South China Seas, and the Sea of Japan (Figure 1). These seas are exposed to a broad spectrum of geological and environmental conditions, ranging from the subtropical to the tropical climatic zones and from the shallow continental shelves to the deep abyssal plains. Better characterization and understanding of the variations of surface winds in recent warming decades is important for modeling and predicting future climate change and impacts on a regional scale.

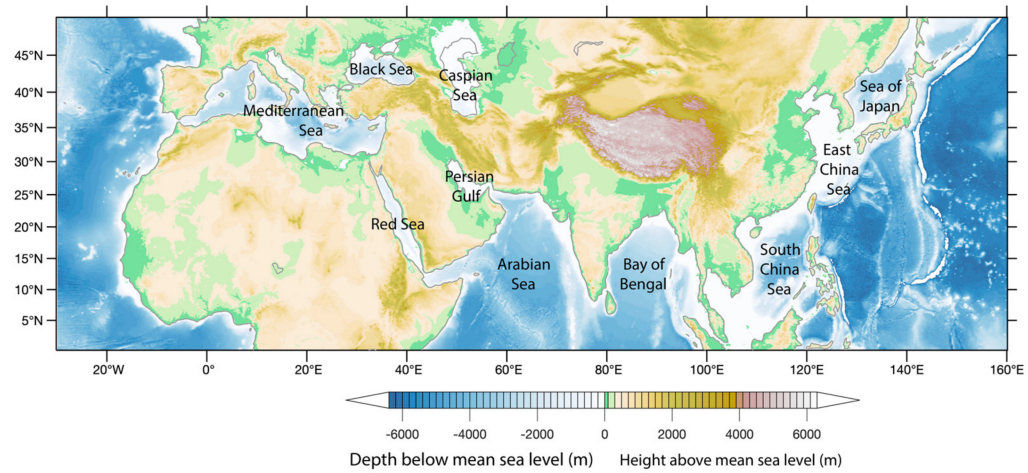

Figure 1. The 10 major semi-enclosed and enclosed marginal seas that surround the Eurasian continent. Left to right: the Mediterranean Sea, the Black Sea, the Caspian Sea, the Red Sea, the Persian Gulf, the Arabian Sea, the Bay of Bengal, the South China Sea, the East China Sea, and the Sea of Japan. The colors denote ocean floor (blues and whites) and land (greens, browns, and purples).

2. Materials and Methods

2.1. Data

The methodology used in developing the OAFlux-HR vector wind analysis stems from the theory of the least-variance linear statistical estimation [41,42]. The formulated least-squares estimator (the so-called cost function) includes data from different sources as well as *a priori* information that one wishes to impose to constrain the solution. The cost function for the OAFlux-HR synthesis, F, is formulated as follows:

$$F = \underbrace{\frac{1}{2}(\vec{V}_a - \vec{V}_b)^T R_b \left(\vec{V}_a - \vec{V}_b\right)}_{(I)} + \underbrace{\frac{1}{2}(\vec{V}_a - \vec{V}_o)^T R_o \left(\vec{V}_a - \vec{V}_o\right)}_{(II)} + \underbrace{\frac{1}{2}(w_a - w_o)^T S_o (w_a - w_o)}_{(III)} + \ldots + \underbrace{\gamma\left(\nabla \times \vec{V}_a - \nabla \times \vec{V}_b\right)^2}_{(IV)} + \underbrace{\lambda\left(\nabla \cdot \vec{V}_a - \nabla \cdot \vec{V}_b\right)^2}_{(V)} \quad (1)$$

where $\vec{V} = (u, v)$ is wind vector with zonal and meridional wind components denoted as u and v, respectively, and $w = \sqrt{u^2 + v^2}$ is wind speed. The superscript "T" denotes transpose, and the subscript "a" denotes an estimate, "b" the background information, and "o" satellite observations. The background information is provided by the bias-corrected atmospheric reanalysis winds from ECMWF Reanalysis-Interim (ERA-interim) [43]. The bias-correction model is a predictor function based on linear regression, in which the coefficients are determined from regression of ERA-interim variables with collocated scat-

terometer retrievals from NSCAT (1995–1996) and SeaWind2 (2002–2003). The background information serves as the first guess when satellite retrievals are missing. The first three terms (I)–(III) are data constraints, and the fourth and fifth terms (IV)–(V) are weak vorticity and divergence constraints [23,44,45]. The matrices *Rb*, *Ro*, and *So* are weighting matrices. The 16 sensors currently included in OAFlux-HR are listed in Table 1, 5 of which are scatterometers (NSCAT, QuikSCAT, OSCAT, ASCAT-A, ASCAT-B) and 11 are microwave radiometers (6 SSM/I, 2 SSMIS, AMSR-E, AMSR2, and WindSat). The methodology, strategy, error estimation, and validation with buoys have been previously published, and readers are referred to references [25,26,30] for details.

Table 1. Characteristics of the 16 sensors included in the OAFlux-HR vector wind synthesis.

Instrument	Platform	Duration	Actual Period in Use	Frequency Band (GHz)	Effective Spatial Resolution along (km) × across (km)	Swath Width (km)	Daily Coverage	Reference
NSCAT	ADEOS-I	15 September 1996–30 June 1997	All	13.995 Ku-band	25 × 25	2 swaths of 600 km	77%	Freilich and Dunbar [20]
QuikSCAT	NASA QuikSCAT	27 October 1999–21 November 2009	All	13.4 Ku-band	25 × 38	1400	92%	Stiles & Dunbar [46]
ASCAT-A	EUMETSAT MetOp series	28 March 2007–present	All	5.255 C-band	12.5 × 12.5	2 swaths of 500 km	71%	Verhoef and Stoffelen [22]
ASCAT-B		29 October 2012–present						
OSCAT	ISRO	23 September 2009–01 April 2014	All	13.5 Ku-band	12.5 × 12.5	1420	92%	Kumar et al. [21]
SSM/I 08	DMSP	9 July 1987–31 December 1991	All	19.35, 22.235, 37.0	69 × 43 50 × 40 37 × 28	1394	75%	Wentz [2]
SSM/I 10	DMSP	8 December 1990–14 November 1997	All					
SSM/I 11	DMSP	3 December 1991–16 May 2000	All					
SSM/I 13	DMSP	3 May 1995–18 November 2009	All					
SSM/I 14	DMSP	8 May 1997–23 August 2008	8 May 1997–31 December 2005					
SSM/I 15	DMSP	18 December 1999–present	18 December 1999–30 June 2006					
SSMIS 16	DMSP	26 October 2003–present	26 October 2003–31 December 2009	19.35 22.235 37.0	69 × 43 50 × 40 37 × 28	1700	80%	
SSMIS 17	DMSP	14 December 2006–present	All					
AMSR-E	NASA Aqua	1 June 2002–4 October 2011	All	18.7 23.8 36.5	27 × 16 32 × 18 14 × 8	1450	77%	
AMSR2	JAXAGCOM-W1	2 July 2012–present	All	10.7 18.7 23.8 36.5	46 × 27 25 × 14 29 × 17 14 × 8	1450	77%	
WindSAT	DoD/Navy Coriolis	5 February 2003–present	*w*: all data *u*,*v*: 05 February 2003–31 December 2013	6.8, 10.7, 18.7, 23.8, 37.0	25 × 38	1025	72%	

2.2. Buoy-Based Validation over the Global Ocean

Validation of the OAFlux-HR vector wind analysis was reported in Yu and Jin [30] using surface wind time-series measurements from 126 moored buoys. Since then, the validation effort has expanded to 30 additional buoys. Some of the additions are from the National Data Buoy Center (NDBC) in near coastal regions and/or at higher latitudes, and some are from the latest field programs including the Ocean Observatories Initiative (OOI), the NASA Salinity Processes in the Upper Ocean Regional Study (SPURS) 1 & 2, the Red Sea buoy established from the partnership between the King Abdullah University of Science and Technology (KAUST) and WHOI [47], the WHOI buoy in the Bay of Bengal [48], and the recently deployed RAMA buoys [49] (Figure 2).

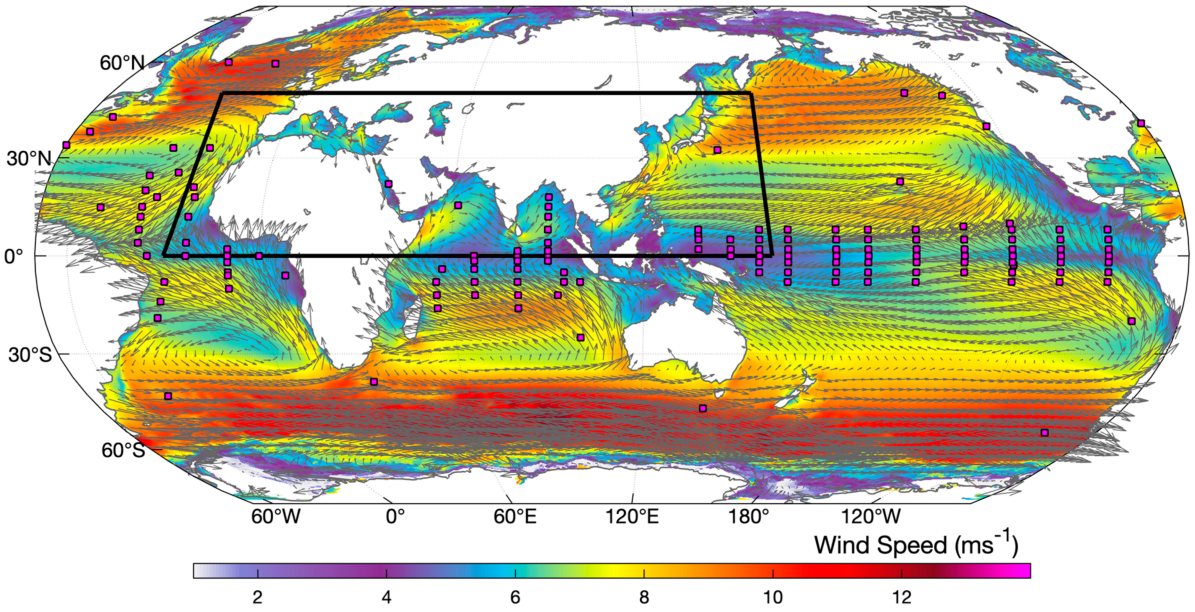

Figure 2. Mean global wind speed (colored background) and direction vector averaged over 1988–2018. The superimposed magenta squares denote the locations of moored surface buoys used as validation (NDBC buoys are not shown). The large black box denotes the focal area of this study.

Buoy winds are sampled by anemometers at the 3–4 m height above the sea surface, and the measurements are transmitted at every 5- or 60-min interval depending upon the design of instruments. The OAFlux-HR wind analysis has daily resolution and is based on satellite wind retrievals that are calibrated to equivalent neutral winds at the 10 m height. For consistency, the high-frequency buoy wind measurements (wind speed, zonal and meridional components) were averaged over each day. These daily buoy winds were then adjusted to the equivalent neutral winds at the 10 m height following Liu and Tang [50]. The conversion requires the near-surface stability information, such as SST, near-surface air temperature, and humidity, and is performed only when buoy measurements of all these variables are available.

Buoy winds are also point measurements and represent time averages over the sample intervals (typically at every 5 or 60 min). Satellite winds are area averages of instantaneously measured winds over the spatial footprint of the satellite. The RMS differences between satellite and buoy measurements could be attributed to both retrieval errors in satellite measurements and sampling errors in buoy measurements of the synoptic wind field.

Furthermore, satellite winds are relative to ocean currents whereas buoy winds are relative to a fixed Earth surface. Kelly et al. [51] showed that satellite wind retrievals are modulated by ocean surface currents. Satellite winds are found to be weaker than buoy winds when the winds are in the same direction as ocean surface currents while stronger than buoy winds when the winds are in the opposite direction to surface currents. The

effect of ocean currents can be a source of bias in assessing the mean differences between satellite and buoy winds [30]. Take the OAFlux-HR u as an example. Table 2 shows that u has a mean bias of -0.17 ms^{-1}, indicating that the satellite-derived u is overall weaker than buoy-measured u in the buoy-covered areas. However, the majority of buoys are from the global tropical moored buoy array [49] (Figure 2), where the westward flowing trade winds drive both the North and South Equatorial Currents westward. Yu and Jin [30] related the mean differences of the collocated satellite-buoy wind pairs to a drifter-derived climatology of near-surface currents [52]. They found that the magnitudes of the satellite-buoy differences are influenced by the speeds and directions of the near-surface currents, and hence, the underestimated bias in OAFlux-HR u may not be an error of the analysis but the effect of ocean currents.

Table 2. Statistics of buoy evaluation of OAFlux-HR w, u, and v.

Wind Component \ Statistics	Total Number of Collocations	Bias (OA-Buoy) (ms^{-1})	RMS (ms^{-1})	CC	R^2 (%)
w	478,334	−0.03	0.77	0.93	87.4
u	468,346	−0.17	1.26	0.95	90.1
v	468,346	0.18	1.17	0.94	88.5

Between 1988 and 2018, the 156 buoy time series produced a total of 478,334 daily values for buoy wind speed and 468,346 daily values for zonal and meridional wind components. Four statistical measures are used to evaluate the accuracy of the OAFlux-HR winds against buoy measurements. The first measure is the mean bias, calculated as the overall daily-mean difference between the collocated OAFlux-HR and buoy winds. The second measure is the root-mean-square (RMS) difference between the two sets of winds, which is expressed as RMS = $\sqrt{\frac{1}{N}\sum_{i=1}^{N}(x_i - x_{bi})^2}$, where N denotes the total number of daily measurements of wind speed (w), zonal and meridional wind components (u and v) over all available buoy locations, x_i is the OAFlux-HR daily wind, and x_{bi} the buoy counterpart. The third measure is the correlation coefficient (CC) that examines the strength of the linear relationship between OAFlux-HR and buoy time series. The last measure is the R-squared value, expressed as $R^2 = \left(1 - \frac{\sum_{i=1}^{N}(x_i - x_{bi})^2}{\sum_{i=1}^{N}(x_i - \overline{x_i})^2}\right) \times 100\%$. The R^2 value is between 0% and 100%, denoting the percent of variation shared between the two sets of winds.

The statistical measures for w, u, and v are summarized in Table 2. OAFlux-HR w has a mean bias of -0.03 ms^{-1} and an rms difference of 0.77 ms^{-1}. The mean bias (rms difference) for u and v is -0.17 (1.26) and 0.18 (1.17) ms^{-1}, respectively. The correlation exceeds 0.93 for all three components. The R^2 value ranges between 87 to 90%. The statistical measures show that the OAFlux-HR winds are in good agreement with the buoy winds.

2.3. OAFlux-HR Wind Comparison with Three Buoys in the Study Domain

Several buoys are located in the Northern Indian Ocean sector of the study domain (Figures 1 and 2). Three buoys deployed by the Upper Ocean Process group at WHOI are selected here to provide in situ insights into the OAFlux-HR winds. They are the Red Sea buoy at 22°N, 39°E [47], the Arabian Sea buoy at 16°N, 62°E [53], and the Bay of Bengal buoy at 18°N, 89°E [48]. The statistical measures with regard to each of the three buoys are listed in Table 3, and the respective daily-mean time-series comparisons are shown in Figures 3–5. It is noted that the three buoys correspond to three different scatterometer periods (Table 1). The Arabian Sea buoy (1994–1995) was in the pre-QuikSCAT period. The Red Sea buoy (2008–2010) covered the transition from QuikSCAT to ASCAT-A and OSCAT. The Bay of Bengal buoy (encompassing the entire 2015) was in the period of ASCAT-A and -B.

Table 3. Statistics of the OAFlux-HR comparison with three selected buoys.

Buoy	Duration	Wind	Bias (OA−Buoy) (ms^{-1})	RMS (ms^{-1})	CC	R^2 (%)
Red Sea 22°N, 39°E	11 October 2008–17 December 2010 N = 797 days	*w*	−0.25	1.00	0.92	84.6
		u	−0.15	1.03	0.91	82.8
		v	− 0.40	1.29	0.93	86.5
Arabian Sea 16°N, 62°E	15 October 1994–10 October 1995 N = 367 days	*w*	−0.91	1.31	0.97	94.1
		u	−0.44	1.15	0.99	98.1
		v	0.01	0.84	0.99	98.4
Bay of Bengal 18°N, 89°E	8 December 2014–30 January 2016 N = 418 days	*w*	−0.06	0.67	0.97	94.3
		u	−0.12	0.82	0.98	96.2
		v	0.35	0.95	0.98	96.5

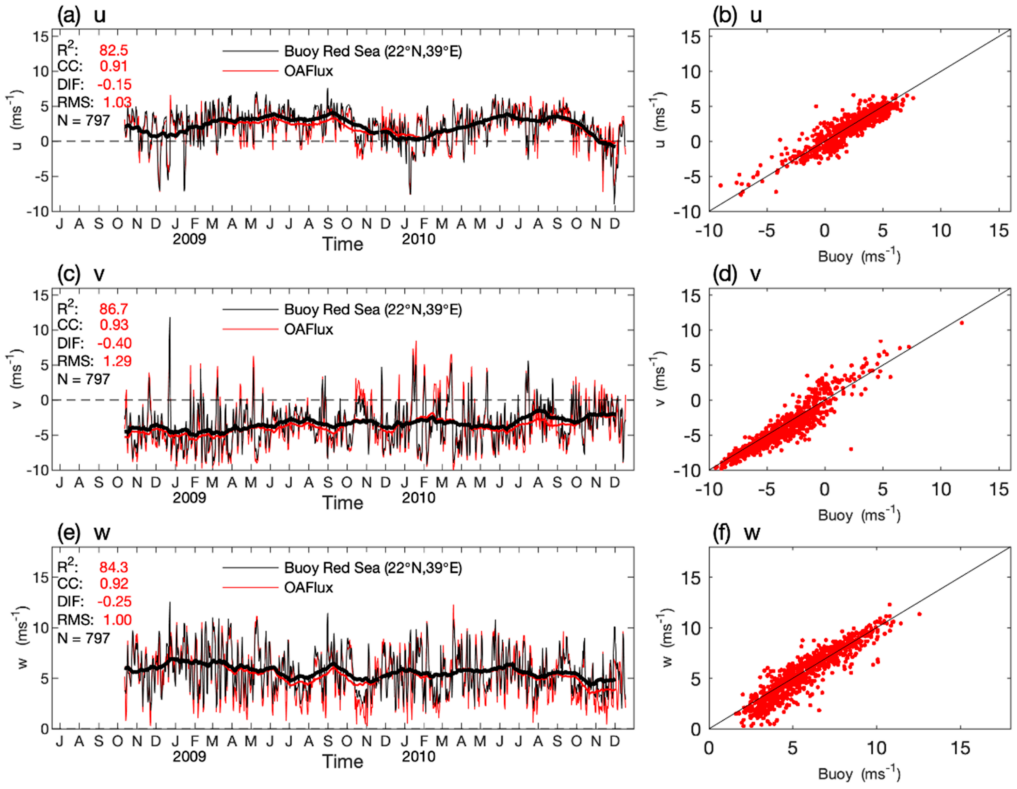

Figure 3. Left column: time series plots of daily buoy winds (thin black) versus OAFlux-HR winds (thin red). Right column: scatter plots of collocated pairs at the Red-Sea buoy location 22°N, 39°E. (**a**,**b**) zonal wind component, (**c**,**d**) meridional wind component, (**e**,**f**) wind speed. Thick smoother lines in (**a**,**c**,**e**) denote a 21-day running mean with black for buoy and red for OAFlux-HR.

The WHOI buoys are equipped with the Improved METeorology (IMET) or Air Sea Interaction–METeorology (ASIMET) systems, and the expected errors are about ± 0.1 m s^{-1} (or 1%) in wind speed and 5° in wind direction [54]. Table 3 shows that the correlations between OAFlux-HR daily winds and buoy daily winds exceed 0.9 at all three sites, and the R^2 values, which represent the variances shared between the two independent sets of daily winds, range from ~84% (Red Sea buoy) to ~98% (Arabian Sea buoy).

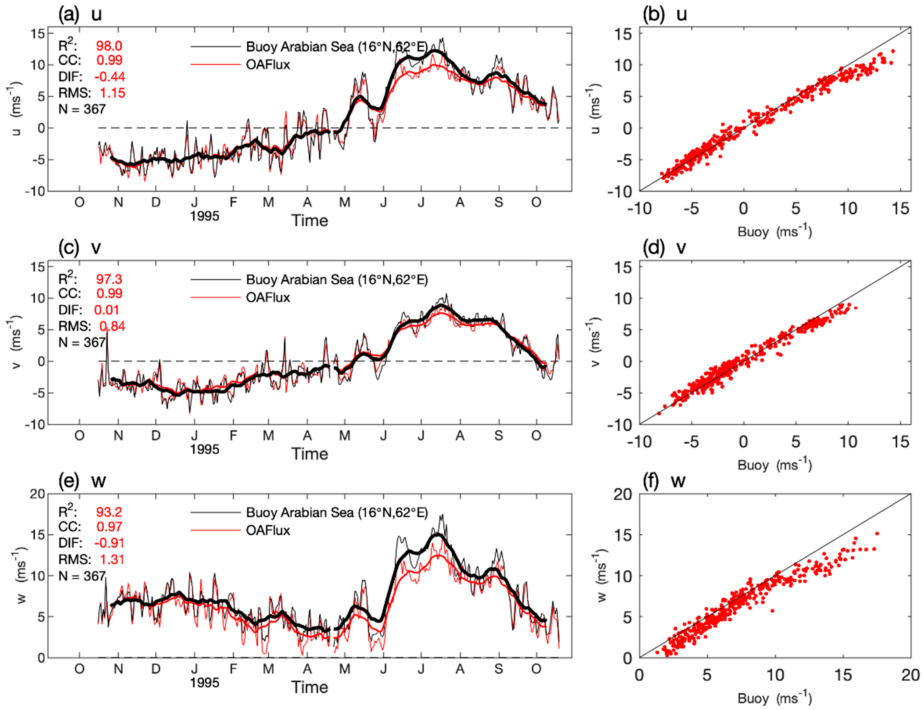

Figure 4. Left column: time series plots of daily buoy winds (thin black) versus OAFlux-HR winds (thin red). Right column: scatter plots of collocated pairs at the Arabian Sea buoy location 16°N, 62°E (**a**,**b**) zonal wind component, (**c**,**d**) meridional wind component, (**e**,**f**) wind speed. Thick smoother lines in (**a**,**c**,**e**) denote a 21-day running mean with black for buoy and red for OAFlux-HR.

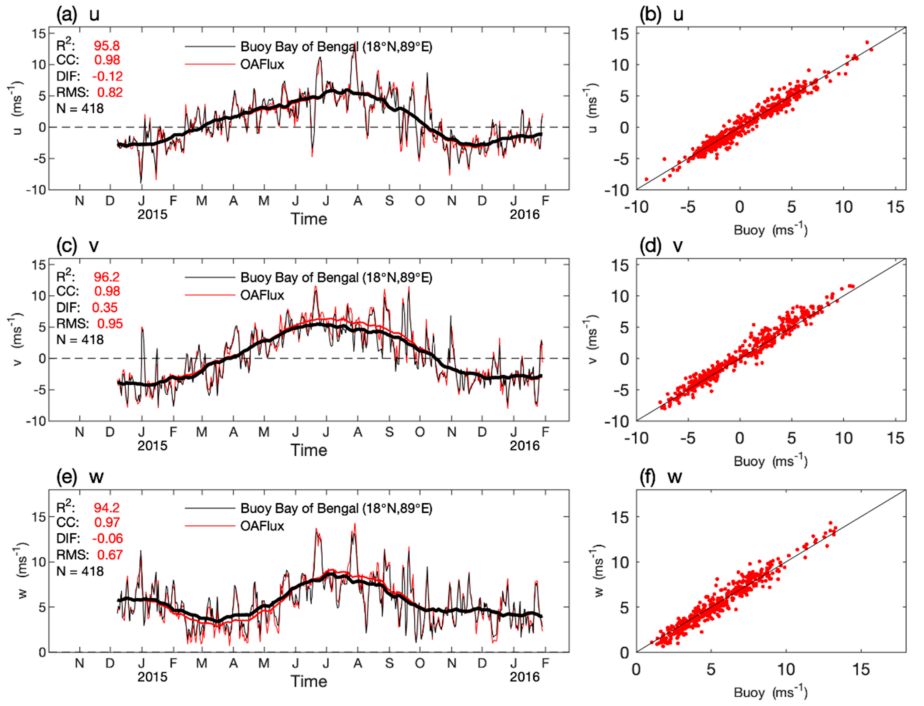

Figure 5. Left column: time series plots of daily buoy winds (thin black) versus OAFlux-HR winds (thin red). Right column: scatter plots of collocated pairs at the Bay of Bengal buoy location 18°N, 89°E. (**a**,**b**) zonal wind component, (**c**,**d**) meridional wind component, (**e**,**f**) wind speed. Thick smoother lines in (**a**,**c**,**e**) denote a 21-day running mean with black for buoy and red for OAFlux-HR.

The Red Sea buoy time series has a duration of approximately two years, while those in the Arabian Sea and the Bay of Bengal are each about one year long. Although the three time series are too short to validate the long-term trends of the OAFlux-HR analysis, they are a valid benchmark for assessing the synoptic-to-seasonal variability in the product. Such information can lead to useful insights into the reliability of the long-term changes in the time series as the trends are generally a manifestation of prolonged changes in the magnitude and/or duration of short-term variability.

Across the three buoy locations (Figures 3–5), the Red Sea buoy winds were relatively weaker with also smaller seasonal variations. The 21-day running mean values indicate that winds were predominantly southeastward throughout the two-year observing period (Figure 3). Seasonal variations were reflected in the changes of u, with the mean value fluctuating about 4 ms^{-1} from May to September and diminishing to near zero during December to February. OAFlux-HR winds perform well at this site. The mean biases are less than 0.4 ms^{-1} for wind speed and components, and the RMS daily mean differences are within 1–1.3 ms^{-1}.

At the Arabian Sea buoy site (Figure 4), the time series shows a distinct seasonal reversal of wind direction that is in line with the monsoonal seasons. Winds flowed southwestward during the winter monsoon from November to February and northeastward during the summer monsoon from June to August. The wind speeds were more intense in the summer monsoon (>12 ms^{-1}) than in the winter monsoon (~7 ms^{-1}) and were weakest during the monsoon transitions (September–October and March–May) (~5 ms^{-1}). Comparing to buoy measurements, OAFlux-HR winds have similar synoptic-seasonal variability but with a slightly lower wind speed. The negative (weak) bias in w (–0.91 ms^{-1}) comes primarily from the bias in u. It appears that OAFlux-HR winds were weaker than buoy winds during the summer monsoon months (June–September) (Figure 4a) due to a weaker bias in both u and v.

The OAFlux-HR winds compare well with the buoy wind measurements at the Bay of Bengal location (Figure 5). The mean bias in w is –0.06 ms^{-1}, which is within the expected accuracy of buoy measurements. The bias is –0.12 ms^{-1} for u and slightly larger for v at about 0.35 ms^{-1}. Similar to the winds at the Arabian Sea site, the winds in the Bay of Bengal strengthened and reversed direction from the winter to summer monsoons. Moreover, the bias in w shows a seasonal dependence: larger in summer when winds were stronger. The cause is not yet known for the seasonally dependent bias in OAFlux-HR winds at the Arabian Sea and Bay of Bengal buoy sites. The retrieval errors in satellite measurements, analysis errors in the synthesis process, sampling errors in buoy measurements, or effects of ocean surface currents could all be potential contributors. Instantaneous surface current measurements at the three buoy sites were not available and their effects could not be evaluated.

3. Results

3.1. Climate Zones and Mean Surface Winds over the Marginal Seas

The 10 marginal and enclosed seas to the south and east of the Eurasian continent (Figure 1) are subject to two unique types of climate conditions. One is the mid-latitude Mediterranean weather pattern that is characterized by warm and dry summers and mild and wet winters [55]. The Mediterranean Sea, the Black Sea, and the Caspian Sea are in this climate zone. The other is the monsoonal weather pattern that is marked by the annual reversal of prevailing wind direction and speed along with contrasting precipitation characteristics. The Arabian Sea and the Bay of Bengal are influenced by the Indian Ocean monsoon, while the South China Sea, the East China Sea, and the Sea of Japan are influenced by the East Asian monsoon. The Indian monsoon and the East Asian monsoon are two components of the Asian Monsoon [56]. The Red Sea and the Persian Gulf reside in the borderline between the mid-latitude and the Indian monsoon influences, though studies have suggested that the mid-latitude forcing has a more dominant influence [57].

In addition to the large-scale climate setting, some of the marginal seas are surrounded by mountain ranges (Figure 1). The interaction between the near-surface airflow and the coastal orography often leads to coastal wind jets, eddies, and gap winds on the meso- and local scales [58]. Hence, the wind pattern in one marginal sea can be distinctly different from the other even though they are in the same climate zone. In the following, the 10 seas are organized into three zones based on the geographic location: the South European marginal seas that include the Mediterranean Sea, the Black Sea, and the Caspian Sea; the North Indian Ocean marginal seas that include the Arabian Sea, the Bay of Bengal, the Red Sea, and the Persian Gulf; and the East Asian marginal seas that include the South China Sea, the East China Sea, and the Sea of Japan.

3.2. Characteristics of Marginal Sea Winds

The spatial pattern of wind speed and direction for the annual mean, the winter season (defined as December-January-February; hereafter DJF) and the summer season (defined as June-July-August, hereafter JJA) is shown in Figure 6a–c, respectively. The standard deviations (STD) of the monthly mean fields were computed for u, v, and w and are shown in Figure 7a–c, respectively. Major characteristics of the surface wind fields for the seas in each of the three climate zones are summarized below.

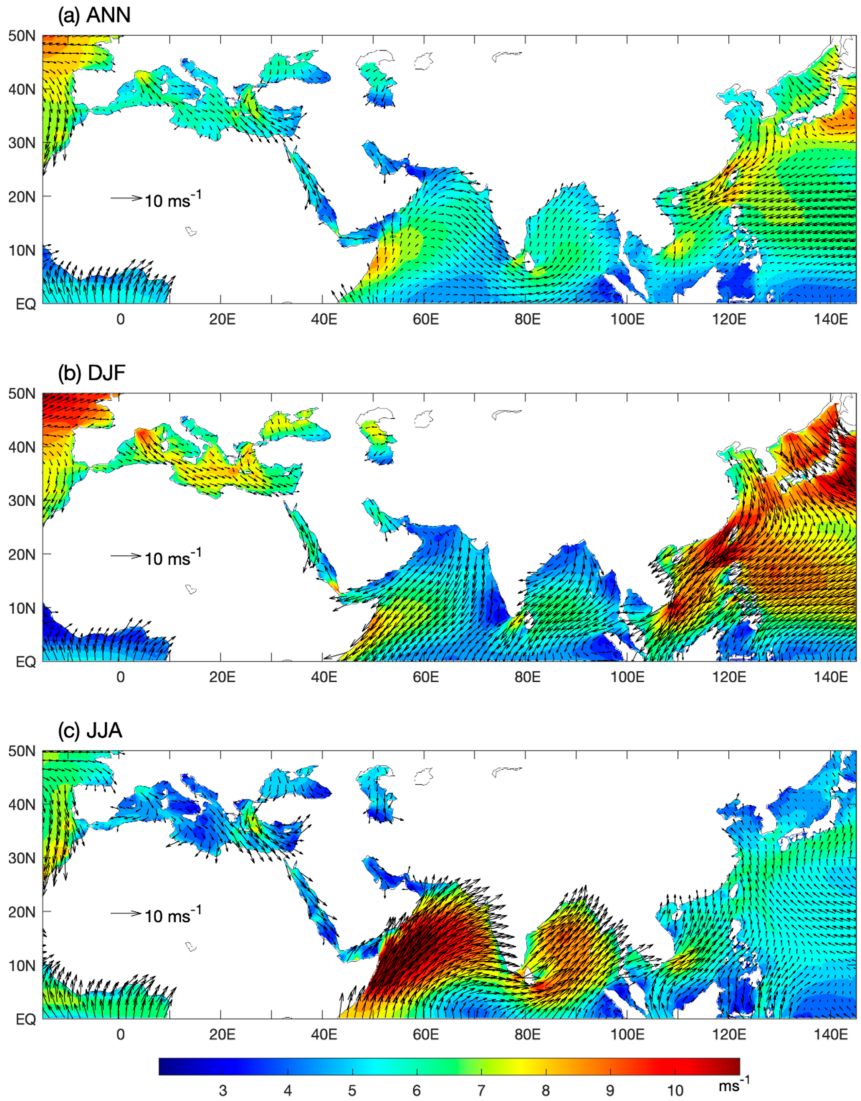

Figure 6. Mean wind speed (shaded by colors) and direction. (**a**) Annual mean, (**b**) winter season (DJF), and (**c**) summer season (JJA).

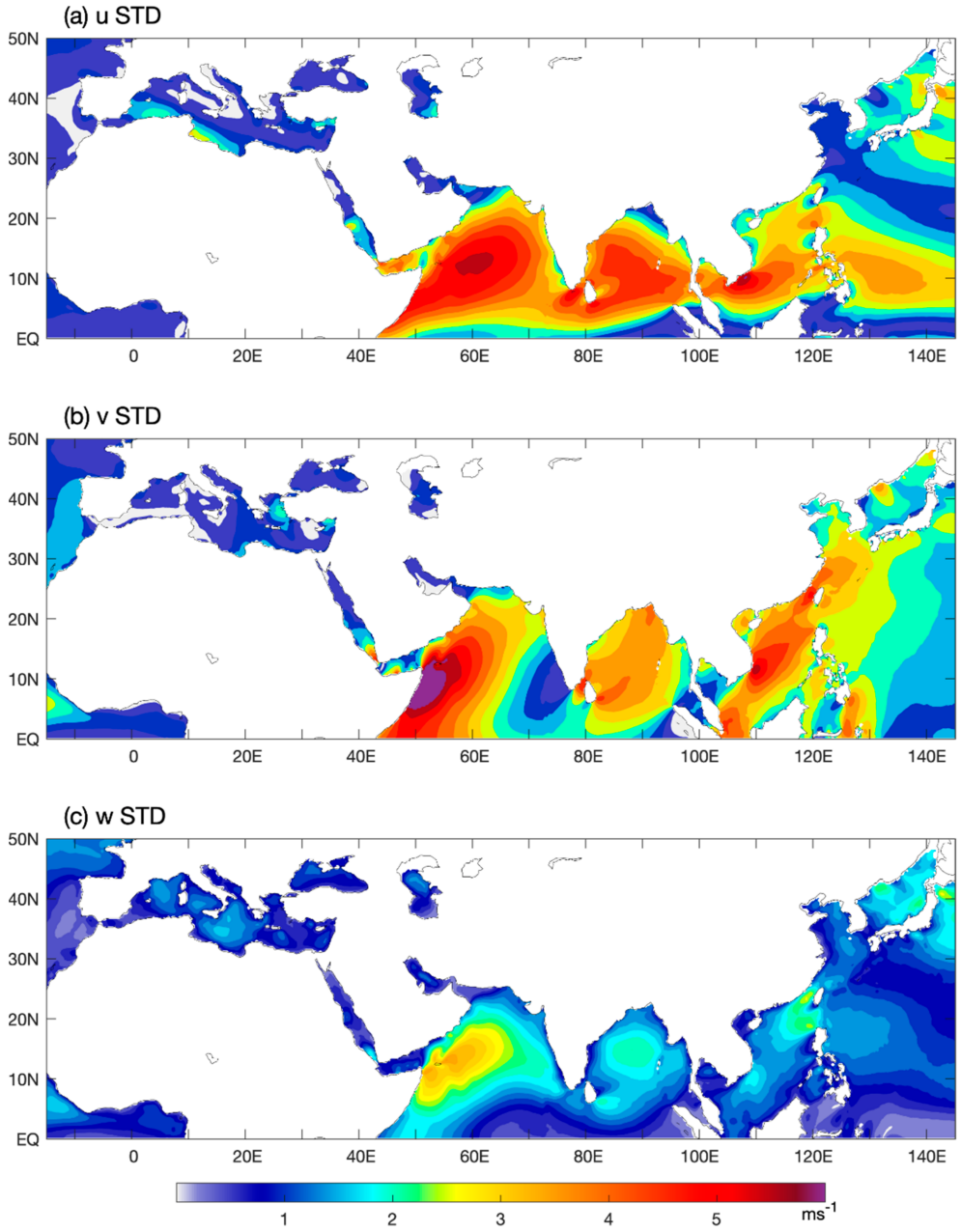

Figure 7. Standard deviation (STD) of seasonal variability of (**a**) zonal wind (u), (**b**) meridional wind (v), and (**c**) wind speed (w).

- The South European marginal seas

The three seas in this climate zone are the Mediterranean Sea, the Black Sea, and the Caspian Sea. The wind pattern in the Mediterranean Sea is strongly influenced by the surrounding mountain ranges [59]. Air flows funnel through the mountain passes to get to the basin from set angles, creating a complex number of local and regional winds with varying strength. On an annual-mean basis (Figure 6a), two persistent regional winds dominant the basin-scale pattern. One is the Mistral, a strong northwesterly jet that blows over the Gulf of Lion and up to the southern Mediterranean shore and the Ionian Sea. The Mistral winds are more prevalent in the winter and spring months (Figure 6b), often creating strong wind bursts that have gale or storm-scale strengths. The other is the Etesian, a northerly wind that prevails in the Aegean Sea and the Eastern Mediterranean during May–October.

The wind system is fairly steady throughout the year. Seasonal STD u is generally weak (<1 ms^{-1}) in the sea, except for the Algerian Basin (the southwest Mediterranean) where winds tend to reverse direction, changing from southeastward in winter to southwestward in summer [60]. Seasonal STD v is also weak on the basin scale, with slightly larger seasonal variability (~2 ms^{-1}) in the Aegean Sea. STD w is at ~1.5 ms^{-1} over most of the western and central basin.

The Black Sea is mostly enclosed by mountains. The surface wind pattern is dominated by the southwesterly from the Mediterranean basin in summer and by the cold northerly and northeasterly from the polar air masses in winter [61,62]. Winds over the western part of the sea are more energetic, where severe storms often occur in winter under the influence of the easterly and northeasterly winds [63]. Winds on the eastern side are light and characterized by more stable conditions. Mean wind speeds are about 8 ms^{-1} in winter and down to about 5 ms^{-1} in summer. Seasonal STD are weak for all components.

Winds in the Caspian Sea vary substantially from north to south [64,65]. The basin in winter is subject to the Siberian high pressure that causes periodic Arctic air mass intrusions. The cold easterly winds induce sea ice to form over the shallow waters in the northernmost region. In summer, the basin is influenced by the Azores high pressure that generates northerly winds of hot, dry air. Wind speeds are typically about 4 ms^{-1} in summer and up to 5–6 ms^{-1} in winter. Similar to the winds over the Mediterranean and Black Seas, the seasonal variability of the winds is relatively weak.

- The North Indian Ocean marginal seas

The four seas in this climate zone are the Arabian Sea, the Bay of Bengal, the Red Sea, and the Persian Gulf. The Arabian Sea and the Bay of Bengal open into the equatorial Indian Ocean in the south. The region is under the influence of the large-scale seasonal atmospheric circulation reversals, featuring southwesterly winds during the summer monsoon (June–September) and northeasterly winds during the winter monsoon (November–February). Winds in summer monsoon are more intense than those in winter monsoon, leading to the dominance of the southwesterly on the annual mean pattern.

Despite the similar large-scale monsoonal setting, the magnitude of w differs between the two basins. The difference is most striking during the summer monsoon, at that time w over the Arabian Sea are more than twice as strong as those over the Bay of Bengal (Figures 4 and 5) with maximum values in the western Arabian Sea near 10°N off the east coast of Somalia. This high w band is associated with the low-level jet that is often referred to as the Findlater jet [66]. The Findlater jet is an atmospheric "western boundary current" similar to that in the oceans [67,68]. It is formed by the orographic dynamics of the East African highlands that bound the Arabian Sea to the west. The annual intensification of the jet is a key feature of the onset of the Indian summer monsoon.

The Red Sea in its full length is surrounded by high mountain ranges (Figure 1). The orographic effects on the regional atmospheric circulation are significant [69], forcing the winds to blow mainly along the axis of the Sea. On synoptic weather time scales, the mountain-gap wind jets often develop from both sides of the central basin, generating winds to blow in a cross-axis direction [70–72]. The mean wind speeds generally increase toward the North. In addition to the continental forcing, the northern basin is influenced by the eastern Mediterranean weather and the southern basin by the Indian monsoons with seasonally reversing winds. The latter is a consequence of the East African highlands, which shield the Gulf of Aden from strong southwest monsoon winds in the summer but steer the northeast monsoon winds into the Gulf of Aden and the southern Red Sea in winter.

The Persian Gulf is less influenced by the Indian monsoons. The winds are predominantly northwesterly throughout the year and are generally light and less variable. The mean w is about 3 ms^{-1} in summer and up to 5 ms^{-1} in winter. Synoptic wind bursts, called Shamal ("North" in the Arabic language), develop in winter seasons in association with mid-latitude disturbances moving from west to east, and these winds often reach gale force and bring dust, cold air, and big seas to the region [73].

- The East Asian marginal seas

Monsoon-related seasonal reversals are the most prominent feature of the winds over the East Asian marginal seas, including the South China Sea, the East China Sea, and the Sea of Japan. A marked seasonality is observed for winds over all seas, weak and variable in summer and strong in winter.

The winter winds blowing over the three-sea system are predominantly northerly, originating from the cold-core Siberia-Mongolia high pressure. Winds over the East China Sea follow closely the basin contours, where the shallow ocean depth enables a strong cold air—warm water coupling [74], which mixes the momentum downward and causes the surface winds to increase when passing through the warm waters. In addition, the orographic effect on the regional winds is evident. Stronger w with a magnitude exceeding 10 ms^{-1} occur in three locations, the Taiwan Strait (~25°N), the Bashi Straits (~21°N), and around 11°N off the southern coast of Vietnam, all of which are attributable to the orographic forcing induced by the surrounding mountains [75,76].

The summer winds are southeasterly in the South China Sea and southerly or southeasterly in the East China Sea and the Sea of Japan. The increasing zonal wind component with latitude reflects the respective tropical and subtropical influence on the broad meridional domain of the East Asian monsoon [77]. The monsoon winds over the South China Sea are tropical in nature, connected to the cross-equatorial flows associated with the western North Pacific monsoon trough (i.e., the Intertropical Convergence Zone (ITCZ)) [78]. When moving northward into the East China Sea and the Sea of Japan, the monsoon winds are affected by a subtropical component that is linked to the subtropical easterly on the western periphery of the western Pacific subtropical high. The winds are generally weaker in summer, with mean w mostly at 5–7 ms^{-1}.

- On the Indian and East Asian monsoons

It is noted that the Indian and East Asian monsoons have different behaviors, although they are two interactive constituents of the Asian Monsoon [56]. In the Indian Ocean, winds are stronger during the summer monsoon, while in the East Asian seas, winds are stronger during the winter monsoon. The differences are caused by several factors, including the different land-sea configurations, the tropical versus subtropical influences, and the atmospheric response to solar heating [78]. For instance, the Indian Ocean seas are located to the south of the Tibetan plateau, and the blocking of the cold Siberian air by the highlands leads to a rather modest winter monsoon. By contrast, the East Asian seas are located to the east of the plateau and exposed directly to the downstream impacts that are driven by the strong contrast between the cold extratropical Asian landmass and the relatively warm North Pacific Ocean. In general, the East Asian monsoon is a complicated system as the result of the land–sea thermal contrast both in the north–south and east–west directions and the dynamic and thermal effects of the Tibetan plateau [79].

3.3. Decadal Changes

Decadal changes in surface wind fields over the 10 marginal seas are examined in terms of linear trends over the length of the time series (Figure 8). Linear trends were estimated by the least-squares regression, and the significance of the trends was evaluated using the Student's t-test by setting the confidence interval to 90%. In the following, the trends labeled with $p < 0.1$ are statistically significant at the 90% confidence interval, and those with $p > 0.1$ are statistically not significant.

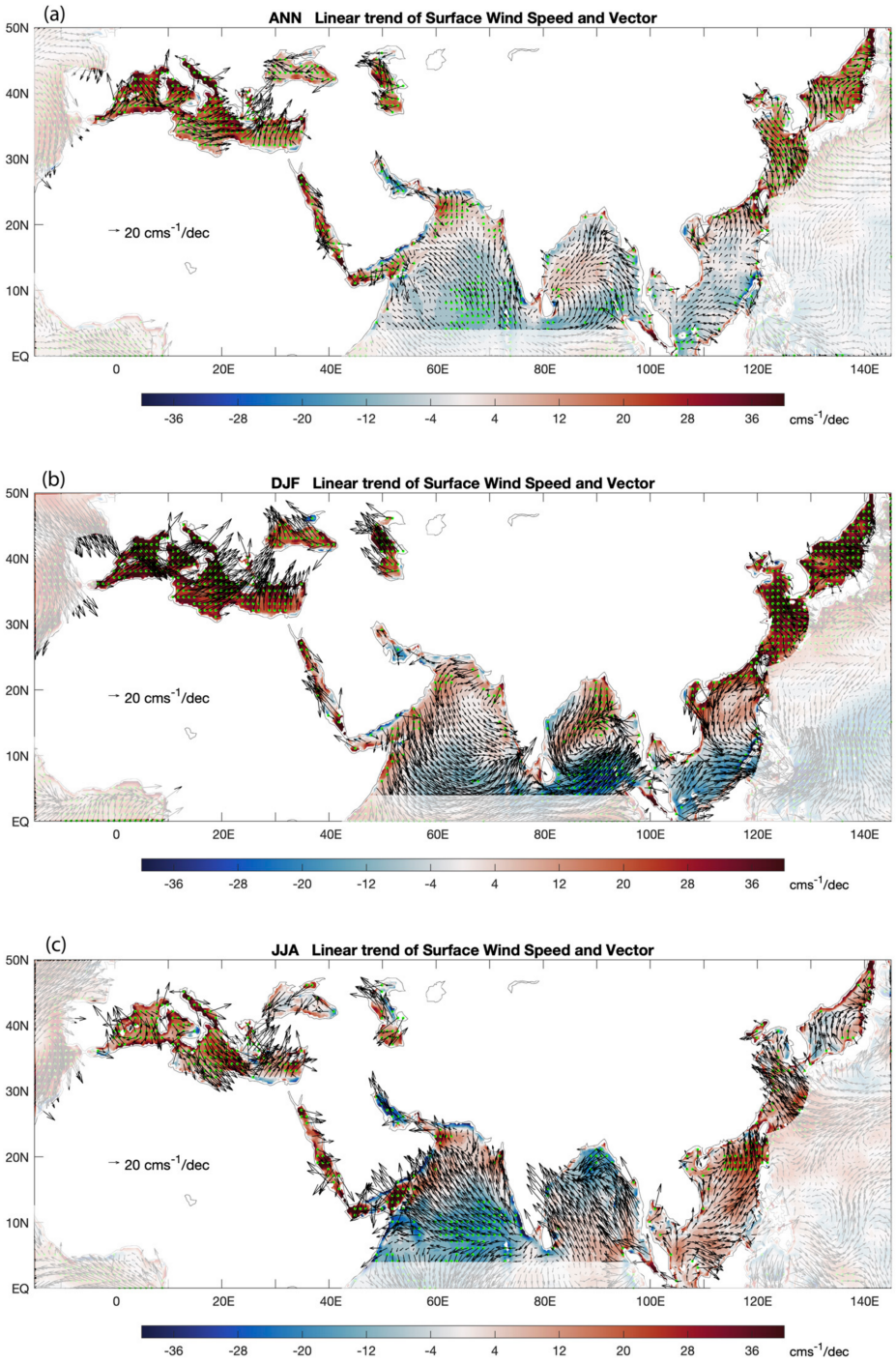

Figure 8. Linear trends of surface wind speed and vector for (**a**) annual mean, (**b**) the winter season (December-January-February), (**c**) the summer season (June-July-August). The green dotted areas denote the linear trends of wind speed that are significant at the 90% confidence interval. The ocean regions outside of the marginal seas are shaded.

The trend maps of the annual-mean w and vector (u, v) (Figure 8a) reveal one striking feature: winds have significantly increased (positive trends) over the seas in the subtropical/mid-latitudes but slightly reduced (negative trends) over the marginal seas in the tropical latitudes. Over three decades, winds have become stronger across the Mediterranean Sea, the Black Sea, the Caspian Sea, and the Red Sea, all of which are under the influence of the Mediterranean weather pattern. The changes of the winds over the

monsoon-influenced seas are less consistent. Winds have strengthened over the East China Sea and the Sea of Japan, where the winds are subject to the influence of both the East Asian monsoon and the western Pacific subtropical high. Winds have weakened over the Arabian Sea, the Bay of Bengal, and the South China Sea, where the monsoon influence is dominant.

The trend maps in winter (DJF) and summer (JJA) are shown in Figure 8b,c, respectively. For most seas, the trend pattern of annual mean winds is dictated primarily by the pattern of change in winter. One exception is the Arabian Sea, where the wind weakening toward the equator is a dominant feature during the summer monsoon. Winds have intensified in both winter and summer over both the South European seas and the North-East Asian seas, but the rate of increase differs considerably between the summer and winter seasons. The rate exceeds 30 cms^{-1} per decade in winter but is less than 15 cms^{-1} per decade in summer, and in some areas, the trends show a change of sign in summer.

To examine the decadal changes in each marginal sea, the trend map of annual-mean wind speed and direction is subsetted for each of the three climate regimes and redrawn using a more refined color code in Figures 9–11. To help identify the seasonal characteristics in these changes, bar plots are drawn to show the basin-averaged linear trends in w for the four seasons: DJF, March-April-May (MAM), JJA, and September-October-November (SON). The characteristic changes over the past three decades are described below.

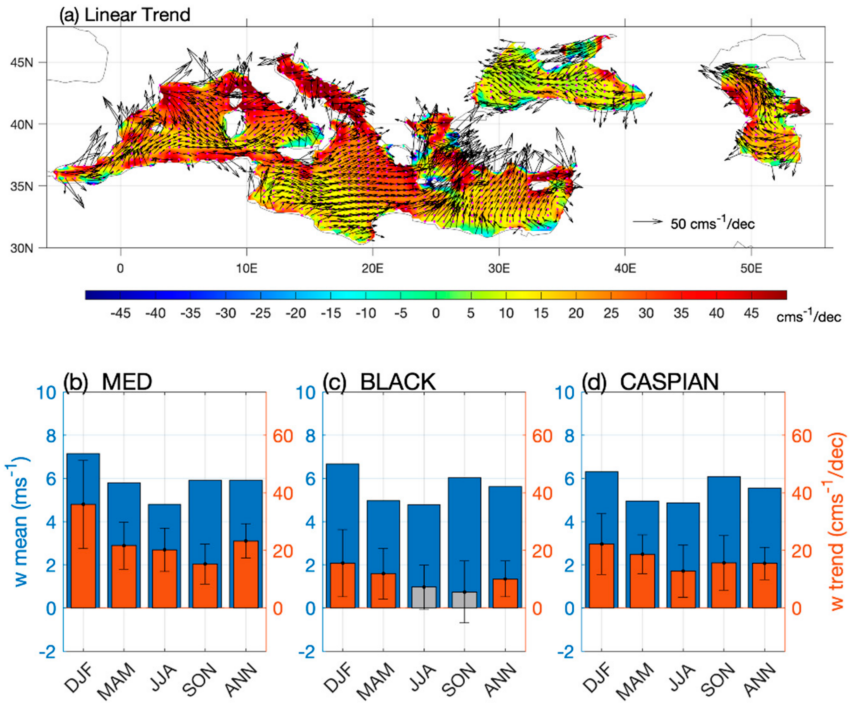

Figure 9. (**a**) Linear trends of annual-mean surface wind speed and vector subsetted from Figure 8a for the South European marginal seas. The magenta dotted areas denote the linear trends of wind speed that are significant at the 90% confidence interval. (**b**–**d**) Bar plots of the basin-averaged mean values (blue bars, left y-axis) and linear trends (red and gray bars, right axis) of wind speed in four seasons: December-January-February (DJF), March-April-May (MAM), June-July-August (JJA), and September-October-November (SON) and the total annual mean (ANN) for (**b**) the Mediterranean Sea (MED), (**c**) the Black Sea (BLACK), and (**d**) the Caspian Sea (CASPIAN). Error bars denote the upper and lower limits of the 90% confidence intervals. Linear trends that are statistically significant (not significant) are colored by red (gray).

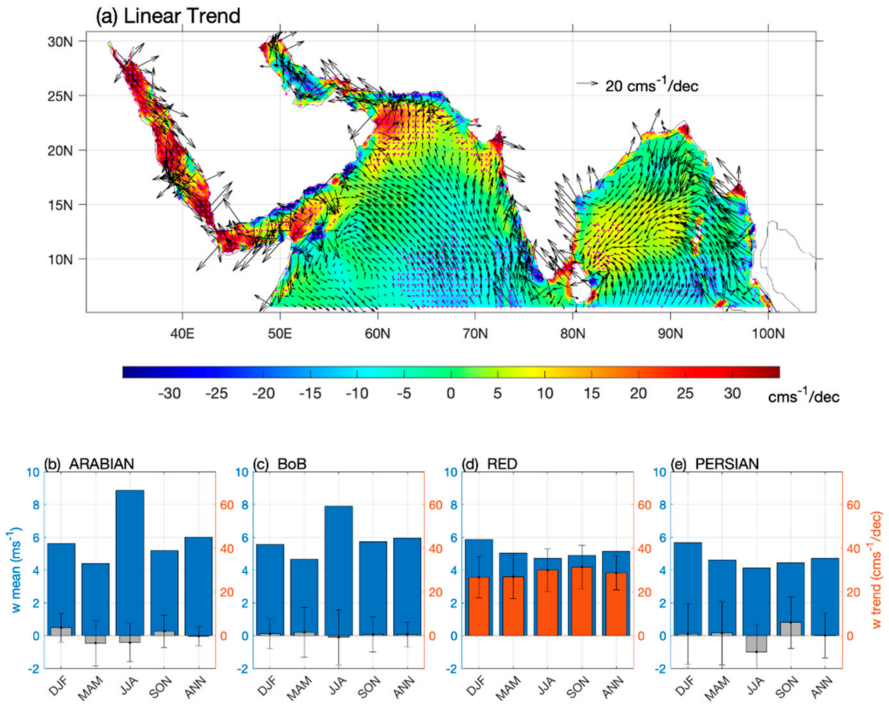

Figure 10. (**a**) Linear trends of annual-mean surface wind speed and vector subsetted from Figure 8a for the North Indian Ocean marginal seas. The magenta dotted areas denote the linear trends of wind speed that are significant at the 90% confidence interval. (**b**–**d**) Bar plots of the basin-averaged mean values (blue bars, left *y*-axis) and linear trends (red and gray bars, right axis) of wind speed in four seasons: December-January-February (DJF), March-April-May (MAM), June-July-August (JJA), and September-October-November (SON) and the total annual mean (ANN) for (**b**) ARABIAN: the Arabian Sea; (**c**) BoB: the Bay of Bengal; (**d**) RED: the Red Sea; and (**e**) PERSIAN: the Persian Gulf. Error bars denote the upper and lower limits of the 90% confidence intervals. Linear trends that are statistically significant (not significant) are colored by red (gray).

- The South European marginal seas

The decadal trends of the winds over the three seas along the southern European continent are shown in Figure 9. The annual-mean winds (Figure 9a) have strengthened in the same direction as the mean winds over the western and central Mediterranean basin but enhanced toward the north and northeast in the eastern basin and the Aegean and Adriatic seas. The rate of increase in w is greater in the northern basin, exceeding 30 cms^{-1} per decade, and less in the southern basin, at about 10 cms^{-1} per decade. The bar plot of the linear trends in Figure 9b shows that winds have strengthened in all seasons, largest in winter (DJF). The overall trend for the annual mean wind speed is statistically significant at about 23 cms^{-1} per decade.

The annual-mean winds in the Black Sea have intensified toward the west, but the rate of increase is smaller compared to that in the Mediterranean Sea. Except for a few localized spots in the eastern basin, the rate of increase in w is mostly around 10 cms^{-1} per decade on the basin scale. The bar plot of the linear trends of w (Figure 9c) indicates that the annual-mean trend pattern reflects mostly the w increase during the winter (DJF) and spring (MAM) seasons, and the changes in summer (JJA) and fall (SON) are not significant. The overall trend for the annual-mean w is upward, at about 11 cms^{-1} per decade.

The annual-mean winds in the Caspian Sea have also increased. The winds have enhanced westward in the southern basin and northwestward in the central basin, with the maximum enhancement occurring in the central basin. Similar to the Mediterranean Sea, the Caspian winds have strengthened in all seasons (Figure 9d) but with a weaker rate. The basin-averaged annual-mean trend is about 17 cms^{-1} per decade.

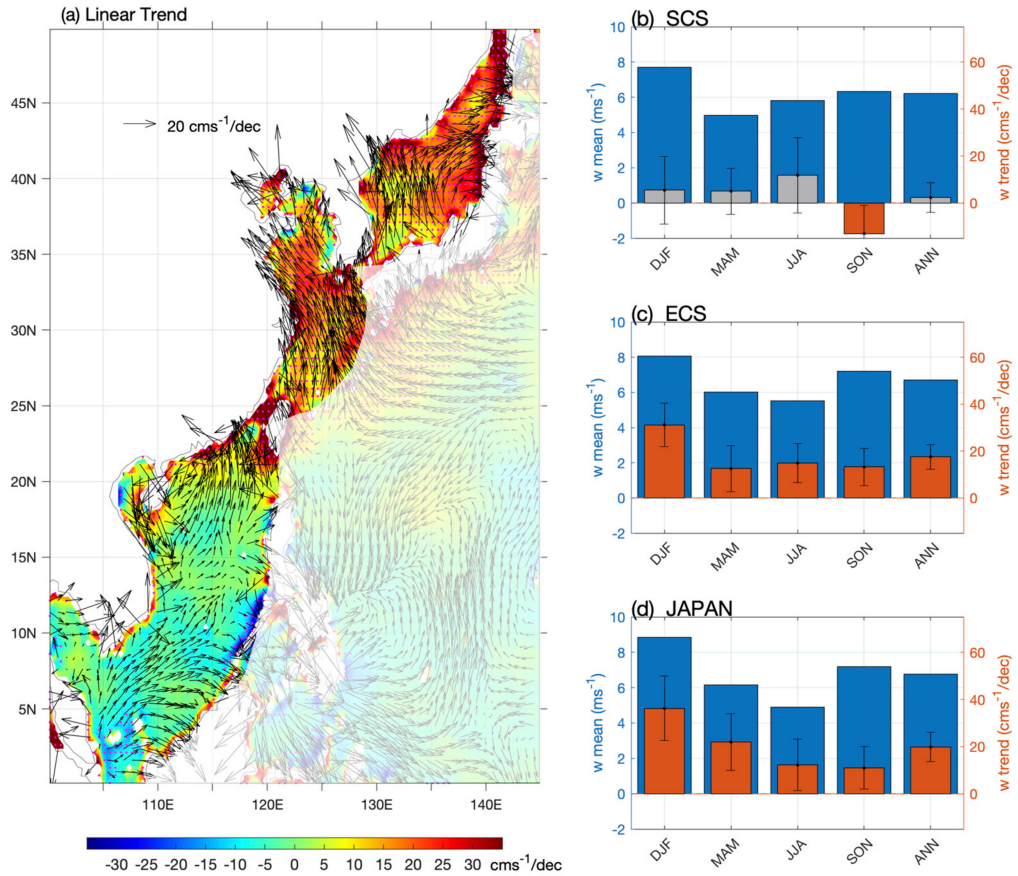

Figure 11. (**a**) Linear trends of annual-mean surface wind speed and vector subsetted from Figure 8a for the East Asian marginal seas. The magenta dotted areas denote the linear trends of wind speed that are significant at the 90% confidence interval. (**b**–**d**) Bar plots of the basin-averaged mean values (blue bars, left *y*-axis) and linear trends (red and gray bars, right axis) of wind speed in four seasons: December-January-February (DJF), March-April-May (MAM), June-July-August (JJA), and September-October-November (SON) and the total annual mean (ANN) for (**b**) A SCS: the South China Sea; (**c**) ECS: the East China Sea; and (**d**) JAPAN: the Sea of Japan. Error bars denote the upper and lower limits of the 90% confidence intervals. Linear trends that are statistically significant (not significant) are colored by red (gray).

- The North Indian Ocean marginal seas

The annual-mean winds have weakened south of 15°N in the Arabian Sea and the Bay of Bengal (Figure 10a). Interestingly, the seasons at which these changes occurred differ between the two basins (Figure 8b,c). In the Arabian Sea, the trend pattern in the winter monsoon is similar to that in the summer monsoon, both featuring negative trends (weakening) in the central and southern basin and positive trends (strengthening) in the northern basin. Reduction in wind speeds is more pronounced in summer and the trends are mostly statistically significant at the 90% confidence interval. In the Bay of Bengal, the trends show a sharp contrast between the northern and southern basins, and the trend patterns reverse the sign from the winter to summer monsoons. Winds in the northern bay have become stronger in the winter monsoon but weaker in the summer monsoon. Conversely, the winds in the southern bay have become weaker in the winter monsoon but stronger in the summer monsoon. The trends in the winter monsoon are more dominant and the pattern is reflected in the annual-mean trend map.

It appears that the Indian summer and winter monsoons may have both been subdued to some degree and the changes have manifested differently in different basins. On a broader scale, the trends in the southern Bay of Bengal are more or less in pace with the

trends in the South China Sea (Figure 8b,c). The seeming connection between these two basins implies that the changes of the winds in the Bay of Bengal may have been governed by a more complex system than those in the Arabian Sea.

The surface winds in the Red Sea have experienced a substantial increase over the past three decades. The winds enhanced predominantly southward in a direction similar to the annual mean winds (Figure 6). By comparison, the Persian Gulf has become a calmer sea. The winds have weakened considerably in the central basin, though the winds near the northern tip of the Gulf have slightly strengthened.

The bar plots in Figure 10b–e show that the basin-averaged trends of w in the Arabian Sea and Bay of Bengal are generally small and not statistically significant for all seasons. This may be due to the cancellation of the positive and negative trends between the northern and southern basins. The averaged trends of w in the Persian Gulf are also small. The Red Sea is the only sea where the upward trends are significant in all months, at about 23 cms^{-1} per decade for annual-mean w.

- The East Asian marginal seas

The trends of the annual-mean winds in the three East Asian marginal seas have considerably different characteristics (Figure 11a). The trends of w are mostly negative in the South China Sea but are overwhelmingly positive in the East China Sea and the Sea of Japan. Moreover, the negative trends in the south are statistically not significant while the positive trends in the north are statistically significant.

The three marginal seas encompass a broad meridional range, extending from the near-equatorial latitudes to mid-latitudes. The trend patterns show that the East Asian monsoon has strengthened, more during winter than during summer (Figure 8b,c). The flow of the trend vectors over the east China Sea in summer had a linkage to the westward enhancement of the winds in the western subtropical North Pacific. It is known that the East Asian summer monsoon has a subtropical component that is sourced from the subtropical easterlies on the western periphery of the western Pacific subtropical high [78]. The enhanced subtropical easterlies over the subtropical western Pacific and marginal seas may indicate a warming-induced local air-sea interaction.

The bar plots (Figure 11b–d) show that the trends in the East China Sea and the Sea of Japan are upward in all seasons, being the largest in winter. The annual-mean trend is about 16 cms^{-1} per decade in the East China Sea and 18 cms^{-1} per decade in the Sea of Japan. The trends in the South China Sea are not significant, except for the fall season (SON) during which the regional winds have weakened.

4. Discussion

The linear trend analysis of the 31-year (1988–2018) time series reveals a striking pattern of wind decadal changes: surface winds strengthening over the marginal seas in the subtropical/mid-latitudes while weakening over the marginal seas in the tropical latitudes. During the analyzed three-decade span, the global climate has alternated between different warming phases: a rapid warming in the 1990s, a warming hiatus in the 2000s, and again a warming acceleration in the 2010s. Given the close coupling between SST and winds on various timescales [39,40], how the changes of surface winds are related to the SST changes are examined below.

4.1. Trends in SST

Linear trends of SST in °C per decade during 1998–2018 are shown in Figure 12. Positive trends are dominant in all 10 marginal seas, and negative trends appear in a few localized areas such as off the northern tip of the Somali coast in the Arabian Sea, the northern East China Sea, and the central Sea of Japan. The rate of warming is larger in the South Europe marginal seas, at about 0.3–0.4 °C per decade in the Mediterranean and Caspian Seas and greater than 0.6 °C per decade in the Black Sea. Considering that the SST over the global ocean increases at an average rate of 0.14 °C per decade during the

same period [80], these marginal and enclosed seas have been warming up at a rate about 2–4 times faster than the global ocean average.

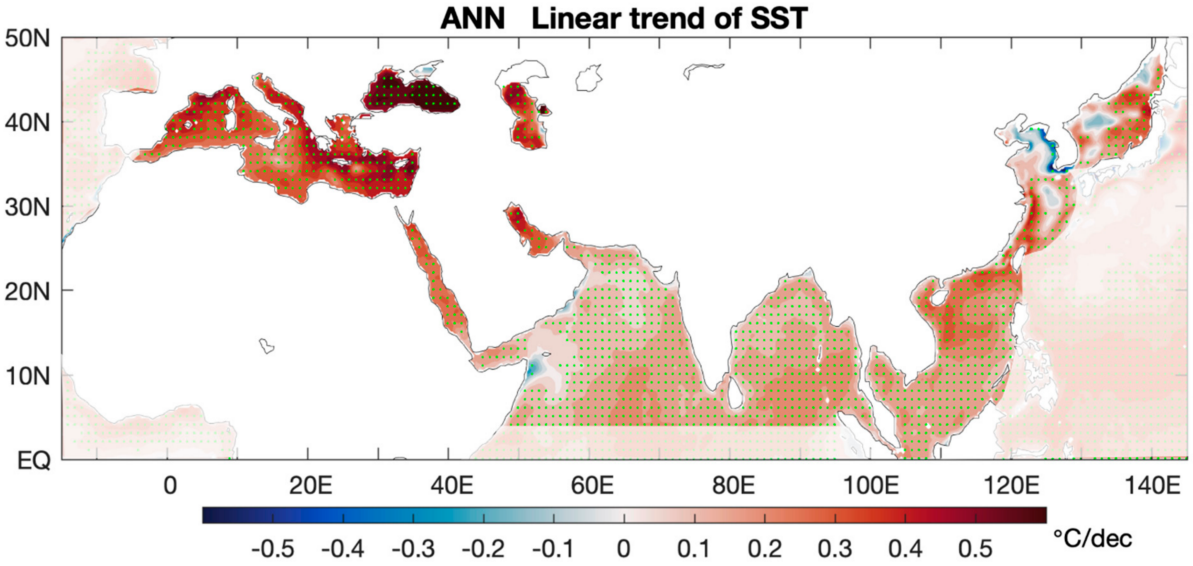

Figure 12. Linear trends of annual mean SST for 1988–2018. The green dotted areas denote the linear trends of wind speed that are significant at the 90% confidence interval. The ocean regions outside of the marginal seas are shaded.

The SSTs in the Red Sea and the Persian Gulf have increased at a rate of ~0.2–0.3 °C per decade. The rate is slightly lower than that in the Mediterranean Sea but certainly higher than the rate of ~0.1 °C per decade in the Arabian Sea and the Bay of Bengal. The SST changes in these two marginal seas seem to align more with the Mediterranean weather pattern than with the monsoon system.

The spatial patterns of SST changes in the East Asian marginal seas are the least uniform comparing to those in the other two climate zones. Areas of negative trends appear in the East China Sea and the Sea of Japan, contrasting to the basin-wide positive trends in the South China Sea. The rate of SST increase in the South China Sea is about 0.1–0.2 °C per decade, similar to that in the Bay of Bengal and the Arabian Sea.

4.2. Decadal Changes in Basin-Averaged SST and Wind Speed

Time series of the basin-averaged annual-mean SST and wind speed constructed for the 10 seas are shown in Figures 13–15 by grouping into three climate zones. Since most time series show a distinct transition around 2000, linear trends for the periods prior to 2000 (1988–2000) and after 2000 (2001–2018) were also estimated. In Figures 13–15, the 31-year trend is denoted by a red solid line and the trends of the two shorter periods by dashed blue lines, with the trend values superimposed. Major characteristics for the SST and wind changes in each zone are summarized as follows.

- The South European marginal seas

The most striking feature in the three SST plots (Figure 13a–c) is the persistent warming trends that have carried through both before and after 2000. The average rate of SST increase is about 0.4 °C per decade in the Mediterranean and Caspian Seas and 0.6 °C per decade in the Black Sea. The Black Sea is the fastest-warming sea among all 10 seas in the study (Figure 12). In the Mediterranean and Black Seas, the rate of SST increase has barely changed before and after 2000. In the Caspian Sea, the rate has decelerated considerably, from ~0.8 °C per decade in the 1990s down to ~0.3 °C per decade in the 2000s–2010s.

The contrasting rate of change before and after 2000 is more evident for wind speed (Figure 13d–f), even for the Mediterranean and Black Seas where the warming trend is persistent. The winds have strengthened at a rate of 11 to 24 cms^{-1} per decade during 1988–

2018 across the three seas. The rates are driven predominantly by the rapid strengthening of surface winds in the 1990s, during which the winds trended up at 31–45 cms^{-1} per decade. After 2000, the trends of wind speed have leveled off.

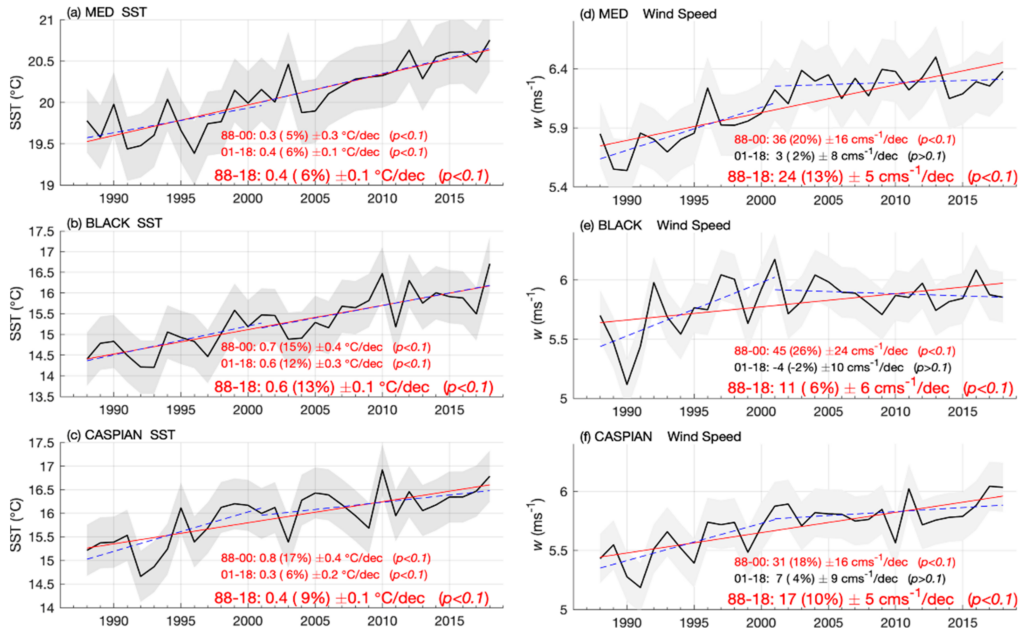

Figure 13. Basin-averaged annual time series (black line) of (**a**–**c**) SST and (**d**–**f**) wind speed for the South European marginal seas. (**a**,**d**) MED: the Mediterranean Sea. (**b**,**e**) BLACK: the Black Sea. (**c**,**f**) CASPIAN: the Caspian Sea. The shaded area denotes one standard deviation of annual-mean variability. The red line denotes the linear trend over 1988–2018, and the dashed blue lines are the linear trends over 1988–2000 and 2001–2018, respectively. Linear trend estimates for the three periods are listed: 1988–2000 (top line), 2001–2018 (middle line), and 1988–2018 (bottom line), colored by red if the trend is statistically significant ($p < 0.1$) or by black if the trend is statistically not significant ($p > 0.1$). The value in the parentheses is the percentage increase.

- The North Indian Ocean marginal seas

SST has increased in all four seas during 1988-2018 (Figure 14a–d), with a larger rate (~0.2 °C per decade) in the Red Sea and the Persian Gulf and a smaller rate (~0.1 °C per decade) in the Arabian Sea and the Bay of Bengal. In the Red Sea and the Persian Gulf, the rate of SST increase in the 1990s (~0.6–1 °C per decade) is at least 3 times faster than that in the two recent decades (~0.2 °C per decade). By contrast, surface warming in the Arabian Sea and the Bay of Bengal did not start until after 2000. The rate of increase is 0.1 °C per decade in the Arabian Sea, and up to about 0.2 °C per decade in the Bay of Bengal. It appears that the Bay of Bengal has warmed up twice as fast as the Arabian Sea in recent decades.

Unlike SST, there is no clear trend in wind speed during 1988–2018 except for the Red Sea (Figure 14e–h). Winds over all four seas had a downward tendency prior to 1998, which is more evident in the Red Sea and the Persian Gulf than in the Arabian Sea and the Bay of Bengal. These downward trends were terminated by an abrupt jump in 2000. Since then, the winds over the four seas have trended in three directions. The first is represented by the winds in the Red Sea, where the trend has held flat after 2000, and the trend of the 31-year period reflects an elevation of the mean wind speed as a result of the sharp change in 2000. The second is represented by the winds over the Persian Gulf, where the trend was flat in the 2000s and then down in the 2010s. The third is characterized by the winds over the Arabian Sea and the Bay of Bengal, where the winds have been less changed despite the increased surface warming in the region.

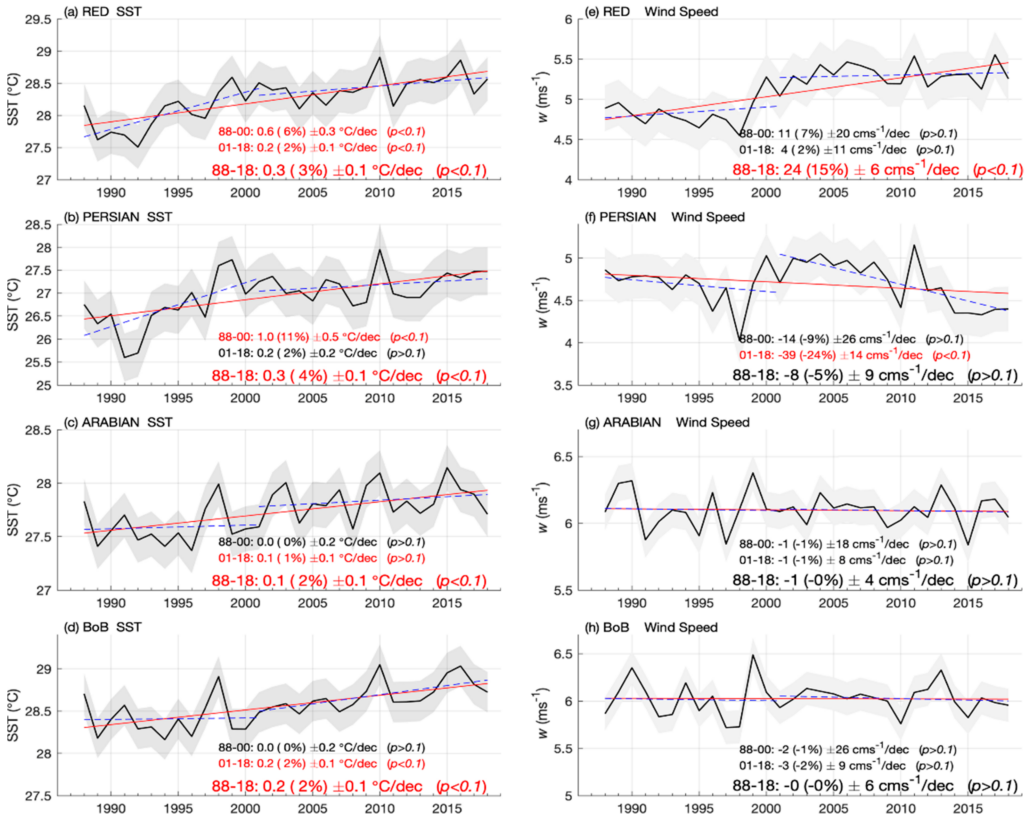

Figure 14. Basin-averaged annual time series (black line) of (**a**–**c**) SST and (**d**–**f**) wind speed for the North Indian Ocean marginal seas. (**a**,**e**) RED: the Red Sea. (**b**,**f**) PERSIAN: the Persian Gulf. (**c**,**g**) ARABIAN: the Arabian Sea. (**d**,**h**) BoB: the Bay of Bengal. The shaded area denotes one standard deviation of annual-mean variability. The red line denotes the linear trend over 1988–2018, and the dashed blue lines are the linear trends over 1988–2000 and 2001–2018, respectively. Linear trend estimates for the three periods are listed: 1988–2000 (top line), 2001–2018 (middle line), and 1988–2018 (bottom line), colored by red if the trend is statistically significant ($p < 0.1$) or by black if the trend is statistically not significant ($p > 0.1$). The value in the parentheses is the percentage increase.

- The East Asian marginal seas

The surface warming trends in the three marginal seas have distinct decadal characteristics (Figure 15a–c). In the South China Sea, the warming has been persistent through the entire 31-year period with a rate of increase at 0.2 °C per decade. In the East China Sea, the SST has trended up rapidly in the 1990s, at a rate of 0.7 °C per decade, but the SST after 2000 is dominated by large interannual variability with no meaningful trend. In the Sea of Japan, the trend has a clear decadal dependence, featuring accelerated warming in the 1990s and a near-flat tendency in the 2000s–2010s.

The annual-mean time series of wind speed (Figure 15d–f) indicate that the winds in the South China Sea have experienced substantial interannual variability but no clear long-term trend during 1988–2018, though the basin has been warming up. The winds in the East China Sea and the Sea of Japan both have strengthened, driven more by the accelerated strengthening in the 1990s. Overall, the winds have increased at 16–18 cms^{-1} per decade in these two seas during 1988–2018.

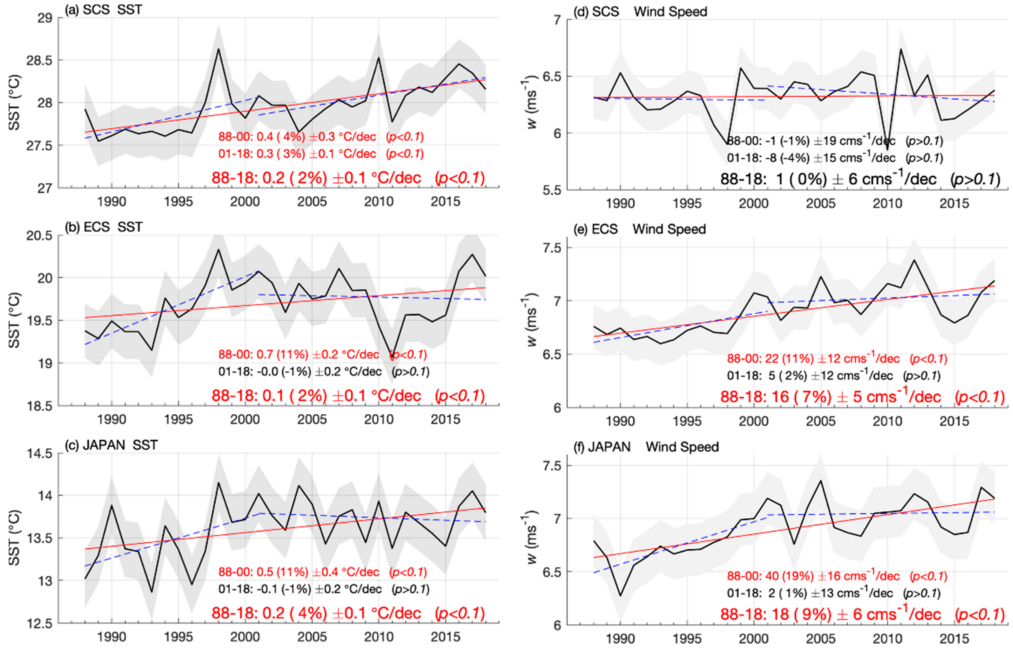

Figure 15. Basin-averaged annual time series (black line) of (**a**–**c**) SST and (**d**–**f**) wind speed for the East Asian marginal seas. (**a**,**d**) SCS: the South China Sea. (**b**,**e**) ECS: the East China Sea. (**c**,**f**) JAPAN: the Sea of Japan. The shaded area denotes one standard deviation of annual-mean variability. The red line denotes the linear trend over 1988–2018, and the dashed blue lines are the linear trends over 1988–2000 and 2001–2018, respectively. Linear trend estimates for the three periods are listed: 1988–2000 (top line), 2001–2018 (middle line), and 1988–2018 (bottom line), colored by red if the trend is statistically significant ($p < 0.1$) or by black if the trend is statistically not significant ($p > 0.1$). The value in the parentheses is the percentage increase.

4.3. Decadal Change Characteristics

To characterize the changes in wind speed and SST, the linear trend estimates listed in Figures 13–15 are tabulated side-by-side in Table 4. Major characteristics of the wind and SST changes for the three periods, 1988–2018, 1988–2000, and 2001–2018, are synthesized as follows.

- The 31-year span (1988–2018)

The basin-averaged SST has increased across the 10 marginal seas, all having statistical significance at the 90% confidence interval. The rate of increase is comparably smaller, about 0.1–0.2 °C per decade, in the five tropical marginal seas under the Asian monsoon influence. These seas include the Arabian Sea, the Bay of Bengal, the South China Sea, the East China Sea, and the Sea of Japan. The warming rate is larger, ranging between 0.4–0.6 °C per decade, for the three south European seas, including the Mediterranean Sea, the Black Sea, and the Caspian Sea. The Red Sea and the Persian Gulf are in the borderline between the Mediterranean weather and the Indian monsoon influences, where the rate of the SST increase is about 0.3 °C per decade, which is also in the midway between the rates in the two climate zones.

Despite the omnipresent warming, the basin-averaged wind speeds have not strengthened everywhere. Winds have become stronger over the marginal seas located in the subtropical/mid-latitudes, including three South European seas (i.e., the Mediterranean, Black, and Caspian seas) and two East Asian seas (i.e., the East China Sea, and the Sea of Japan), and the rate of increase ranges between 11–24 cms^{-1} per decade. Winds over the marginal seas in the tropical latitudes under the monsoon influence have slightly weakened or little changed, except for the Red Sea where the winds have increased at a rate of 24 cms^{-1} per decade.

Table 4. Linear trend estimates of the annual-mean wind speed in the 10 marginal seas for three periods: 1988–2018, 1988–2000, 2001–2018. The trends that are statistically significant at the 90% confidence interval are highlighted by bold numbers. The confidence limit shown as error bars. MED: the Mediterranean Sea; BLACK: the Black Sea; and CASPIAN: the Caspian Sea; RED: the Red Sea; PERSIAN: the Persian Gulf; ARABIAN: the Arabian Sea; BoB: the Bay of Bengal; SCS: the South China Sea; ECS: the East China Sea; JAPAN: the Sea of Japan.

Marginal Sea	Trend 1988–2018		Trend 1988–2000		Trend 2001–2018	
	SST (°C/dec)	Wind Speed (cms^{-1}/dec)	SST (°C/dec)	Wind Speed (cms^{-1}/dec)	SST (°C/dec)	Wind Speed (cms^{-1}/dec)
MED	**0.4 ± 0.1**	**24 ± 5**	**0.3 ± 0.3**	**36 ± 16**	**0.4 ± 0.1**	3 ± 8
BLACK	**0.6 ± 0.1**	**11 ± 6**	**0.7 ± 0.4**	**45 ± 24**	**0.6 ± 0.3**	−4 ± 10
CASPIAN	**0.4 ± 0.1**	**17 ± 5**	**0.8 ± 0.4**	**31 ± 16**	**0.3 ± 0.2**	7 ± 9
RED	**0.3 ± 0.1**	**24 ± 6**	**0.6 ± 0.3**	11 ± 20	**0.2 ± 0.1**	4 ± 11
PERSIAN	**0.3 ± 0.1**	−8 ± 9	**1.0 ± 0.5**	−14 ± 26	0.2 ± 0.2	**−39 ± 24**
ARABIAN	**0.1 ± 0.1**	−1 ± 4	0.0 ± 0.2	−1 ± 18	**0.1 ± 0.1**	−1 ± 8
BoB	**0.2 ± 0.1**	−0 ± 6	0.0 ± 0.2	−2 ± 26	**0.2 ± 0.1**	−3 ± 9
SCS	**0.2 ± 0.1**	1 ± 6	**0.4 ± 0.3**	−1 ± 19	**0.3 ± 0.1**	−8 ± 15
ECS	**0.1 ± 0.1**	**16 ± 5**	**0.7 ± 0.2**	**22 ± 12**	−0.0 ± 0.2	5 ± 12
JAPAN	**0.2 ± 0.1**	**18 ± 6**	**0.5 ± 0.4**	**40 ± 16**	−0.1 ± 0.2	2 ± 13

- The 1990s (1988–2000)

SST has increased at a faster rate in the 1990s in all marginal seas except for the Arabian Sea and the Bay of Bengal, where the basin-averaged SST show no obvious trend. In the other seas, the rate of increase ranges from 0.3 to 1 °C per decade. The wind speeds over the five seas in the subtropical/mid-latitudes have increased, at a rate of 22–45 cms^{-1} per decade. The winds over the marginal seas in the tropical latitudes have slightly weakened, but the trends are statistically not significant.

- The 2000s and 2010s (2001–2018)

SST has continued to increase in the three South European seas, the Red Sea, and the Persian Gulf, though at a smaller rate of increase (0.2–0.6 °C per decade) comparing to that in the 1990s. In the Arabian Sea and the Bay of Bengal, the surface has started to warm up at a rate of 0.1–0.2 °C per decade. The surface warming has continued in the South China Sea but ceased in the East China Sea and the Sea of Japan. By comparison, the trends of wind speeds have leveled off over all seas, except for the Persian Gulf that shows a strong reduction in wind speeds.

- Synopsis

Although the SST trends through the entire 31-year period are all upward in the 10 marginal seas, the upward trends in the Arabian Sea and the Bay of Bengal are due to the warming that started after 2000 while the trends in the other 8 seas are driven by accelerated warming in the 1990s. The surface winds have also experienced two distinct decadal phases over the 31-year span. The strengthening of the surface winds over the five mid-latitude marginal seas in the 1990s has receded after 2000. The winds over the three tropical marginal seas have weakened only slightly throughout the 31-year period. The wind changes over the Red Sea and the Persian Gulf reflect a regime shift in the regional mean wind speeds.

4.4. Decadal Change Patterns

A map based on the sign and statistical significance of the trends (Table 4) was constructed for SST and wind speed for the three respective periods: 1988–2018, 1988–2000, and 2001–2018 (Figure 16). It shows that the relationship between wind and SST changes is highly nonlinear and varies with the basin. The wind changes are related to the SST changes in three distinct ways. First, the winds over the South European marginal seas

increased with the rising SST in the 1990s but remained near-steady after 2000 despite the continuation of the surface warming trend. Second, the basin-averaged wind speeds in the Arabian Sea and the Bay of Bengal experienced little decadal trends either before or after 2000, although the SST has been trending upward after 2000. Lastly, the East China Sea and the Sea of Japan are the only seas where SST and wind changes have positive correlations, both of which have trended upward in the 1990s and flattened in the 2000s–2010s.

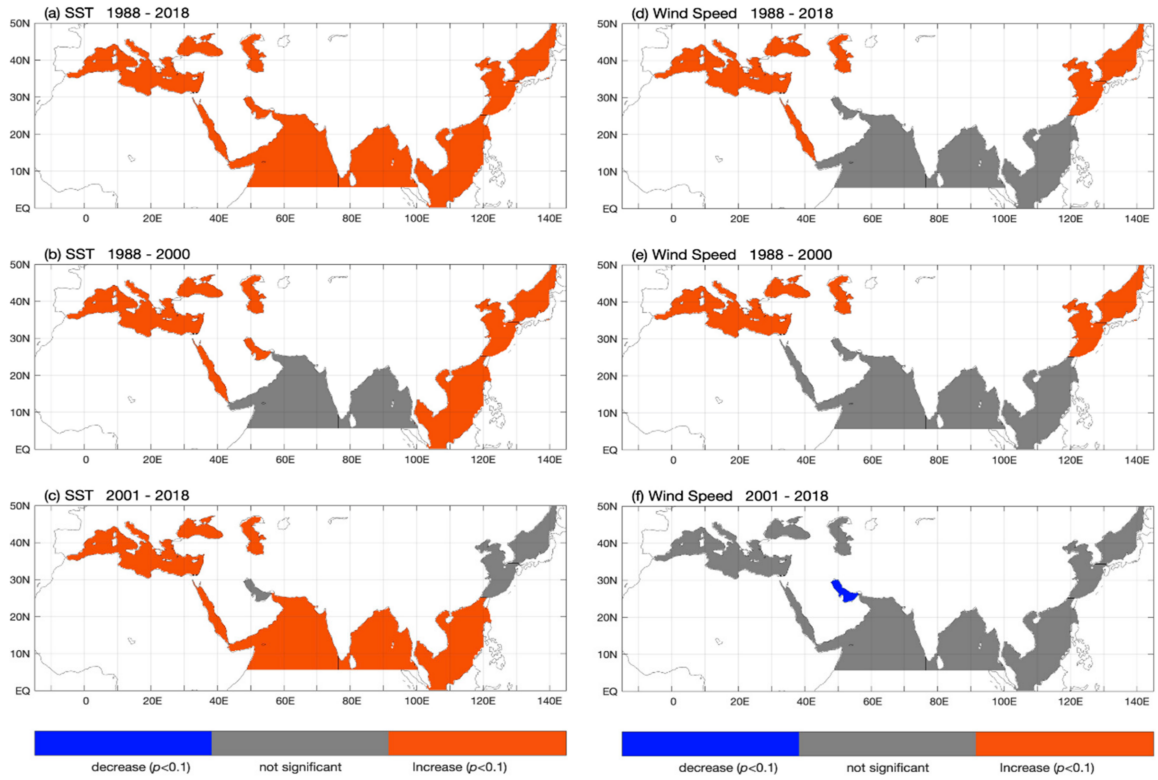

Figure 16. Schematic depiction of the decadal changes in annual-mean winds averaged over each of the 10 marginal seas for SST (left) and wind speed (right) in three periods: (**a**,**d**): 1988–2018; (**b**,**e**): 1988–2000; (**c**,**f**): 2001–2018. Areas colored in red (blue) denote that the rate of increase (reduction) in SST and wind speeds is statistically significant at the 90% confidence interval. The areas colored in gray denote that the changes in the SST or wind speed are not significant.

5. Conclusions

This study utilizes satellite observations of the past three decades (1988–2018) to provide the first full characterization of decadal variations of surface winds over 10 marginal seas surrounding the Eurasian continent. During the three decades, the global climate has alternated between different warming phases: rapid warming in the 1990s, a warming hiatus in the 2000s, and a warming acceleration again in the 2010s. The average rate of SST increase is about 0.12 °C per decade over the global ocean [80]. This study finds that surface warming has occurred across the 10 marginal seas over the 31-year span, more pronounced in the South European Seas (0.4–0.6 °C per decade) than in the North Indian and East Asian marginal Seas (0.1–0.2 °C per decade). The rate of SST increase in the South European seas is about 3–5 times higher than the rate of the global ocean average.

At the same time, surface winds have not increased everywhere. On basin average, winds have strengthened over the five marginal seas in the subtropical mid-latitudes, including the Mediterranean Sea, the Black Sea, the Caspian Sea, the East China Sea, and the Sea of Japan, with the rate of increase ranging between 11–24 cms^{-1} per decade. These trends are driven predominantly by the accelerated changes in the 1990s, during which the winds strengthened at a rate almost twice the 31-year mean rate. Surface winds have slightly weakened over the marginal seas in the tropical region that is influenced by the

monsoon, including the Arabian Sea, the Bay of Bengal, and the South China Sea, but the trends are weak and statistically not significant. The winds over the Red Sea and the Persian Gulf underwent an abrupt shift in 2000 that elevated the mean wind speed to a new regime. Trends have largely flattened over most of the seas during the warming of the most recent decade.

The varying relationships between wind and SST changes suggest that different marginal seas have responded differently to warming. The 10 marginal seas are exposed to a broad spectrum of environmental, orographic, and weather conditions, and differ in size and the volume to surface area ratio. The spatial variability in their responses is a complex outcome of the interaction between local thermal and orographic forcing and air-sea processes. The study is ongoing to investigate and understand the physical drivers of the change of the near-surface atmospheric circulation and to identify key air-sea mechanisms in each marginal sea. Such study will be useful for improving the understanding of the regional response to global climate change, and for improving the projection of future climate change and impacts on the marginal seas.

Funding: This research was funded by NASA Making Earth System Data Records for Use in Research Environments (MEaSUREs) program, grant number 80NSSC18M0079, NASA Ocean Vector Wind Science Team (OVWST) program, grant number NNX14AL82G, and NOAA Global Ocean Monitoring and Observation (GOMO) Program, grand number NA19OAR4320074.

Institutional Review Board Statement: Not applicable.

Informed Consent Statement: Not applicable.

Data Availability Statement: Publicly available datasets were analyzed in generating the OAFlux-HR datasets presented in this study. All OAFlux products are publicly accessible at http://oaflux.whoi.edu (accessed on 5 April 2021). The OAFlux-HR datasets for this study are currently available on request from the corresponding author and will be disseminated through the project website.

Acknowledgments: The satellite wind products of SSM/I, SSMIS AMSRE, AMSR2, and WindSat were downloaded from Remote Sensing Systems at http://www.ssmi.com/ (accessed on 5 April 2021). ASCAT-A&B datasets were downloaded from NASA JPL PO.DAAC at http://podaac.jpl.nasa.gov (accessed on 5 April 2021), and the original ASCAT datasets are hosted by KNMI at http://www.knmi.nl/scatterometer (accessed on 5 April 2021). Oceansat-2 and QuikSCAT were from NASA JPL PO.DAAC at https://podaac.jpl.nasa.gov/ (accessed on 5 April 2021). We thank all data providers for making the high-quality data available for this research. Buoy measurements from the TAO, PIRATA, and RAMA programs were downloaded from http://pmel.noaa.gov (accessed on 5 April 2021). The WHOI KAUST, Bay of Bengal, and Arabian Sea buoys were from http://uop.whoi.edu (accessed on 5 April 2021). The NDBC buoys were from http://www.ndbc.noaa.gov (accessed on 5 April 2021).

Conflicts of Interest: The authors declare no conflict of interest.

References

1. Hollinger, J.P.; Peirce, J.L.; Poe, G.A. SSM/I Instrument Evaluation. *IEEE Trans. Geosci. Remote Sens.* **1990**, *28*, 781–790. [CrossRef]
2. Wentz, F.J. A well-calibrated ocean algorithm for SSM/I. *J. Geophys. Res.* **1997**, *102*, 8703–8718. [CrossRef]
3. Kunkee, D.B.; Poe, G.A.; Boucher, D.J.; Swadley, S.D.; Hong, Y.; Wessel, J.E.; Uliana, E.A. Design and evaluation of the First Special Sensor Microwave Imager/Sounder. *IEEE Trans. Geosci. Remote Sens.* **2008**, *46*, 863–883. [CrossRef]
4. Young, I.R.; Zieger, S.; Babanin, A.V. Global trends in wind speed and wave height. *Science* **2011**, *332*, 451–455. [CrossRef]
5. Yu, L.; Weller, R.A. Objectively Analyzed air-sea heat Fluxes (OAFlux) for the global ocean. *Bull. Am. Meteor. Soc.* **2007**, *88*, 527–539. [CrossRef]
6. Wentz, F.J.; Ricciardulli, L.; Hilburn, K.; Mears, C. How much more rain will global warming bring? *Science* **2007**, *317*, 233–235. [CrossRef]
7. Yu, L. Global variations in oceanic evaporation (1958-2005): The role of the changing wind speed. *J. Clim.* **2007**, *20*, 5376–5390. [CrossRef]
8. Huntington, T.G. Evidence for intensification of the global water cycle: Review and synthesis. *J. Hydrol.* **2006**, *319*, 83–95. [CrossRef]
9. Zieger, S.; Babanin, A.V.; Young, I.R. Changes in ocean surface wind with a focus on trends in regional and monthly mean values. *Deep-Sea Res. I* **2014**, *86*, 56–67. [CrossRef]

10. Milliff, R.F.; Morzel, J. The global distribution of the time-average wind stress curl from NSCAT. *J. Atmos. Sci.* **2001**, *58*, 109–131. [CrossRef]
11. Sturges, W.; Douglas, B.C. Wind effects on estimates of sea level rise. *J. Geophys. Res.* **2011**, *116*, C06008. [CrossRef]
12. Toggweiler, J.R. Shifting westerlies. *Science* **2009**, *323*, 1434–1435. [CrossRef]
13. England, M.H.; McGregor, S.; Spence, P.; Meehl, G.A.; Timmermann, A.; Cai, W.; Gupta, A.S.; McPhaden, M.J.; Purich, A.; Santoso, A. Recent intensification of wind-driven circulation in the Pacific and the ongoing warming hiatus. *Nat. Clim. Chang.* **2014**, *4*, 222–227. [CrossRef]
14. Trenberth, K.E.; Guillemot, C.J.; Stepaniak, D. The atmospheric energy budget and implications for surface fluxes and ocean heat transports. *Clim. Dyn.* **2001**, *17*, 259–276. [CrossRef]
15. Villas Bôas, A.B.; Ardhuin, F.; Ayet, A.; Bourassa, M.A.; Brandt, P.; Chapron, B.; Cornuelle, B.D.; Farrar, J.T.; Fewings, M.R.; Fox-Kemper, B.; et al. Integrated observations of global surface winds, currents, and waves: Requirements and challenges for the next decade. *Front. Mar. Sci.* **2019**, *6*, 425. [CrossRef]
16. Spencer, M.W.; Wu, C.; Long, D.G. Improved resolution back scatter measurements with the SeaWinds pencil-beam scatterometer. *IEEE Trans. Geosci. Remote Sens.* **2000**, *38*, 89–103. [CrossRef]
17. Figa-Saldaña, J.; Wilson, J.J.; Attema, E.; Gelsthorpe, R.; Drinkwater, M.R.; Stoffelen, A. The advanced scatterometer (ASCAT) on the meteorological operational (MetOp) platform: A follow on for European wind scatterometers. *Can. J. Remote Sens.* **2002**, *28*, 404–412. [CrossRef]
18. Naderi, F.M.; Freilich, M.H.; Long, D.G. Spaceborne radar measurement of wind velocity over the ocean-an overview of the NSCAT scatterometer system. *Proc. IEEE* **1991**, 850–866. [CrossRef]
19. Freilich, M.H.; Long, D.G.; Spencer, M.W. SeaWinds: A scanning scatterometer for ADEOS-II-science overview. In Proceedings of the IGARSS'94 IEEE International Geoscience and Remote Sensing Symposium, Pasadena, CA, USA, 8–12 August 1994; Volume 2, pp. 960–963. [CrossRef]
20. Freilich, M.H.; Dunbar, R.S. The accuracy of the NSCAT vector winds: Comparisons with national data buoy center buoys. *J. Geophys. Res. Oceans* **1999**, *104*, 11231–11246. [CrossRef]
21. Kumar, K.; Bhowmick, S.A.; Babu, K.N.; Nigam, R.; Sarkar, A. Relative calibration of scatterometer backscattering coefficient using natural land targets-A preparatory study for OCEANSAT-2 scatterometer. *IEEE Trans. Geosci. Remote Sens.* **2011**, *49*, 2268–2273. [CrossRef]
22. Verhoef, A.H.; Stoffelen, A.C.M. *ASCAT WindProduct User Manual Version 1.15*. SAF/OSI/CDOP/KNMI/TEC/MA/126, EUMETSAT. 2018. Available online: http://projects.knmi.nl/publications/fulltexts/ss3_pm_ascat_1.15.pdf (accessed on 5 April 2021).
23. Atlas, R.; Hoffman, R.N.; Ardizzone, J.; Leidner, S.M.; Jusem, J.C.; Smith, D.K.; Gombos, D. A cross-calibrated, multiplatform ocean surface wind velocity product for meteorological and oceanographic applications. *Bull. Am. Meteorol. Soc.* **2011**, *92*, 157–174. [CrossRef]
24. Bentamy, A.; Grodsky, S.A.; Carton, J.A.; Croizé-Fillon, D.; Chapron, B. Matching ASCAT and QuikSCAT winds. *J. Geoph. Res.* **2012**, *117*, C02011. [CrossRef]
25. Yu, L.; Jin, X. Insights on the OAFlux ocean surface vector wind analysis merged from scatterometers and passive microwave radiometers (1987 onward). *J. Geophys. Res. Oceans* **2014**, *119*, 5244–5269. [CrossRef]
26. Yu, L.; Jin, X. Confidence and sensitivity study of the OAFlux multi-sensor synthesis of the global ocean-surface vector wind from 1987 onward. *J. Geophys. Res. Oceans* **2014**, *119*, 6842–6862. [CrossRef]
27. Wentz, F.J.; Ricciardulli, L.; Rodriguez, E.; Stiles, B.W.; Bourassa, M.A.; Long, D.G.; Hoffman, R.N.; Stoffelen, A.; Verhoef, A.; O'Neill, L.W.; et al. Evaluating and extending the ocean wind climate data record. *IEEE J. Sel. Top Appl. Earth Obs. Remote Sens.* **2017**, *10*, 2165–2185. [CrossRef]
28. Tomita, H.; Hihara, T.; Kako, S.; Kubota, M.; Kutsuwada, K. An introduction to J-OFURO3: A third-generation Japanese ocean flux data set using remote-sensing observations. *J. Oceanogr.* **2019**, *75*, 171–194. [CrossRef]
29. Yu, L. Global air-sea fluxes of heat, fresh water, and momentum: Energy budget closure and unanswered questions. *Annu. Rev. Mar. Sci.* **2019**, *11*, 227–248. [CrossRef]
30. Yu, L.; Jin, X. Buoy perspective of a high-resolution global ocean vector wind analysis using passive radiometers and active scatterometers from 1987 to the present. *J. Geophys. Res.* **2012**, *117*, C11013. [CrossRef]
31. Schroeder, K.; Chiggiato, J.; Josey, S.A.; Borghini, M.; Aracri, S.; Sparnocchia, S. Rapid response to climate change in a marginal sea. *Sci. Rep.* **2017**, *7*, 4065. [CrossRef]
32. Bai, Y.; He, X.; Yu, S.; Chen, C.-T.A. Changes in the ecological environment of the marginal seas along the Eurasian continent from 2003 to 2014. *Sustainability* **2018**, *10*, 635. [CrossRef]
33. Rostov, I.D.; Dmitrieva, E.V.; Rudykh, N.I.; Vorontsov, A.A. Climatic changes in thermal conditions of marginal seas in the western Pacific. *Russ. Meteorol. Hydrol.* **2020**, *45*, 169–178. [CrossRef]
34. Marbà, N.; Jordà, G.; Agustí, S.; Girard, C.; Duarte, C.M. Footprints of climate change on Mediterranean Sea biota. *Front. Mar. Sci.* **2015**, *2*, 56. [CrossRef]
35. Vargas-Yanez, M.; García, M.J.; Salat, J.; García-Martínez, M.C.; Pascual, J.; Moya, F. Warming trends and decadal variability in the western Mediterranean shelf. *Glob. Planet. Chang.* **2008**, *63*, 177–184. [CrossRef]
36. Diffenbaugh, N.S.; Pal, J.S.; Giorgi, F.; Gao, X. Heat stress intensification in the Mediterranean climate change hotspot. *Geophys. Res. Lett.* **2007**, *34*, L11706. [CrossRef]

37. Alawad, K.A.; Al-Subhi, A.M.; Alsaafani, M.A.; Alraddadi, T.M. Decadal variability and recent summer warming amplification of the sea surface temperature in the Red Sea. *PLoS ONE* **2020**, *15*, e0237436. [CrossRef]
38. Raitsos, D.E.; Hoteit, I.; Prihartato, P.K.; Chronis, T.; Triantafyllou, G.; Abualnaja, Y. Abrupt warming of the Red Sea. *Geophys. Res. Lett.* **2011**, *38*, L14601. [CrossRef]
39. Lindzen, R.S.; Nigam, S. On the role of sea surface temperature gradients in forcing low level winds and convergence in the tropics. *J. Atmos. Sci.* **1987**, *44*, 2418–2436. [CrossRef]
40. Wallace, J.M.; Mitchell, T.P.; Deser, C. The influence of sea surface temperature on surface wind in the eastern equatorial Pacific: Seasonal and interannual variability. *J. Clim.* **1989**, *2*, 1492–1499. [CrossRef]
41. Daley, R. *Atmospheric Data Analysis*; Cambridge University Press: Cambridge, UK, 1991; 457p.
42. Talagrand, O. Assimilation of observations, an Introduction. *J. Meteorol. Soc. Jpn.* **1997**, *75*, 191–209. [CrossRef]
43. Dee, D.P.; Uppala, S.M.; Simmons, A.J.; Berrisford, P.; Poli, P.; Kobayashi, S.; Andrae, U.; Balmaseda, M.A.; Balsamo, G.; Bauer, P.; et al. The ERA-Interim reanalysis: Configuration and performance of the data assimilation system. *Quart. J. R. Meteorol. Soc.* **2011**, *137*, 553–597. [CrossRef]
44. Hoffman, R.N. SASS wind ambiguity removal by direct minimization. Part II: Use of smoothness and dynamical constraints. *Mon. Wea. Rev.* **1984**, *112*, 1829–1852. [CrossRef]
45. Stoffelen, A.; Anderson, D. Ambiguity removal and assimilation of scatterometer data. *Q. J. R. Meteo. Soc.* **1997**, *123*, 491–518. [CrossRef]
46. Stiles, B.W.; Dunbar, R.S. A neural network technique for improving the accuracy of scatterometer winds in rainy conditions. *IEEE Trans. Geosci. Remote Sens.* **2010**, *48*, 3114–3122. [CrossRef]
47. Farrar, J.T.; Lentz, S.; Churchill, J.; Bouchard, P.; Smith, J.; Kemp, J.; Lord, J.; Allsup, G.; Hosom, D. *King Abdullah University of Science and Technology (KAUST) Mooring Deployment Cruise and Field-Work Report, Technical Report*; Woods Hole Oceanographic Institute: Woods Hole, MA, USA, 2009; 88p, Available online: http://uop.whoi.edu/projects/kaust/docs/KAUST2009Cruise.pdf (accessed on 5 April 2021).
48. Weller, R.A.; Farrar, J.T.; Buckley, J.; Mathew, S.; Venkatesan, R.; Sree Lekha, J.; Chaudhuri, D.; Suresh Kumar, N.; Praveen Kumar, B. Air-sea interaction in the Bay of Bengal. *Oceanography* **2016**, *29*, 28–37. [CrossRef]
49. McPhaden, M.; Ando, K.; Bourlès, B.; Freitag, H.P.; Lumpkin, R.; Masumoto, Y.; Murty, V.S.N.; Nobre, P.; Ravichandran, M.; Vialard, J.; et al. The Global Tropical Moored Buoy Array. In Proceedings of the OceanObs'09: Sustained Ocean Observations and Information for Society, Venice, Italy, 21–25 September 2009; ESA Publication WPP-306. Hall, J., Harrison, D.E., Stammer, D., Eds.; 2009; Volume 2. Available online: https://www.aoml.noaa.gov/phod/docs/McPhaden_TheGlobalTropical.pdf (accessed on 5 April 2021). [CrossRef]
50. Liu, W.T.; Tang, W. *Equivalent Neutral Wind*; Jet Propulsion Laboratory Tech., Rep. 96-17; Jet Propulsion Laboratory, California Institute of Technology: Pasadena, CA, USA, 1996; 20p. Available online: https://ntrs.nasa.gov/api/citations/19970010322/downloads/19970010322.pdf?attachment=true (accessed on 26 April 2021).
51. Kelly, K.A.; Dickinson, S.; McPhaden, M.J.; Johnson, G.C. Ocean currents evident in satellite wind data. *Geophys. Res. Lett.* **2001**, *28*, 2469–2472. [CrossRef]
52. Lumpkin, R.; Garraffo, Z. Evaluating the decomposition of tropical Atlantic drifter observations. *J. Atmos. Oceanic Tech.* **2005**, *22*, 1403–1415. [CrossRef]
53. Weller, R.A.; Baumgartner, M.F.; Josey, S.A.; Fischer, A.S.; Kindle, J.C. Atmospheric forcing in the Arabian Sea during 1994-1995: Observations and comparisons with climatology and models. *Deep-Sea Res. II* **1998**, *45*, 1961–1999. [CrossRef]
54. Colbo, K.; Weller, R.A. The accuracy of the IMET sensor package in the subtropics. *J. Atmos. Oceanic Technol.* **2009**, *26*, 1867–1890. [CrossRef]
55. Lionello, P. *Malanotte-Rizzoli, P., Boscolo, R. Mediterranean Climate Variability*; Elsevier: Amsterdam, The Netherlands, 2006; 438p.
56. Wang, B. *The Asian Monsoon*; Springer: New York, NY, USA; Praxis Publishing Co.: New York, NY, USA, 2005; 787p.
57. Langodan, S.; Cavaleri, L.; Vishwanadhapalli, Y.; Pomaro, A.; Bertotti, L.; Hoteit, I. The climatology of the Red Sea—Part 1: The wind. *Int. J. Climatol.* **2017**, *37*, 4509–4517. [CrossRef]
58. National Research Council. *Coastal Meteorology: A Review of the State of the Science*; The National Academies Press: Washington, DC, USA, 1992. [CrossRef]
59. Jervis, W.W. Mediterranean climate—Its variants and transitional types. *Geogr. Teach.* **1925**, *13*, 126–129.
60. Tyrlis, E.; Lelieveld, J. Climatology and dynamics of the summer Etesian winds over the Eastern Mediterranean. *J. Atmos. Sci.* **2013**, *70*, 3374–3396. [CrossRef]
61. Zecchetto, S.; De Biasio, F. Sea surface winds over the Mediterranean basin from satellite data (2000-04): Meso-and local-scale features on annual and seasonal time scales. *J. Appl. Meteor. Climatol.* **2007**, *46*, 814–827. [CrossRef]
62. Efimov, V.; Shokurov, M. Spatiotemporal structure of the surface wind field over the Black Sea. *Izv. Acad. Sci. USSR Atmos. Oceanic Phys.* **2002**, *38*, 421–430.
63. Onea, F.; Rusu, E. Wind energy assessments along the Black Sea basin. *Met. Apps.* **2014**, *21*, 316–329. [CrossRef]
64. Rusu, E. Evaluation of the wave energy conversion efficiency in various coastal environments. *Energies* **2014**, *7*, 4002–4018. [CrossRef]
65. Arpe, K.; Molavi-Arabshahi, M.; Leroy, S.A.G. Wind variability over the Caspian Sea, its impact on Caspian seawater level and link with ENSO. *Int. J. Climatol.* **2020**, *40*, 6039–6054. [CrossRef]

66. Findlater, J. A major low-level air current near the Indian Ocean during the northern summer. *Q. J. R. Meteorol. Soc.* **1969**, *95*, 362–380. [CrossRef]
67. Anderson, D.L.T. The low-level jet as a western boundary current. *Mon. Wea. Rev.* **1976**, *104*, 907–921. [CrossRef]
68. Slingo, J.; Spencer, H.; Hoskins, B.; Berrisford, P.; Black, E. The meteorology of the western Indian Ocean, and the influence of the East African Highlands. *Philos. Trans. A. Math. Phys. Eng. Sci.* **2005**, *363*, 25–42. [CrossRef]
69. Patzert, W.C. Wind-induced reversal in Red Sea circulation. *Deep-Sea Res.* **1974**, *21*, 109–121. [CrossRef]
70. Jiang, H.; Farrar, J.T.; Beardsley, R.C.; Chen, R.; Chen, C. Zonal surface wind jets across the Red Sea due to mountain gap forcing along both sides of the Red Sea. *Geophys. Res. Lett* **2009**, *36*, L19605. [CrossRef]
71. Bower, A.S.; Farrar, J.T. Air-sea interaction and horizontal circulation in the Red Sea. In *The Red Sea*; Rasul, N.M.A., Stewart, I.C.F., Eds.; Springer: Berlin/Heidelberg, Germany, 2015; pp. 329–342.
72. Menezes, V.V.; Farrar, J.T.; Bower, A.S. Westward mountain-gap wind jets of the northern Red Sea as seen by QuikSCAT. *Remote Sens. Environ.* **2018**, 677–699. [CrossRef]
73. Perrone, T. *Winter Shamal in the Persian Gulf*; Technical Report 79-06; Naval Environmental Prediction Research Facility: Monterey, CA, USA, 1979; p. 180. Available online: https://apps.dtic.mil/dtic/tr/fulltext/u2/a077727.pdf (accessed on 5 April 2021).
74. Xie, S.-P.; Hafner, J.; Tanimoto, Y.; Liu, W.T.; Tokinaga, H.; Xu, H. Bathymetric effect on the winter sea surface temperature and climate of the Yellow and East China Seas. *Geophys. Res. Lett.* **2002**, *29*, 2228. [CrossRef]
75. Liu, W.T.; Xie, X. Space-based observations of the seasonal changes of South Asian monsoons and oceanic response. *Geophys. Res. Lett.* **1999**, *26*, 1473–1476. [CrossRef]
76. Xie, S.-P.; Xie, Q.; Wang, D.; Liu, W.T. Summer upwelling in the South China Sea and its role in regional climate variations. *J. Geophys. Res.* **2003**, *108*, 3261. [CrossRef]
77. Trenberth, K.E.; Stepaniak, D.P.; Caron, J.M. The Global monsoon as seen through the divergent atmospheric circulation. *J. Clim.* **2000**, *13*, 3969–3993. [CrossRef]
78. Ding, Y.H.; Chan, J.C.L. The East Asian monsoon: An overview. *Meteor. Atmos. Phys.* **2005**, *89*, 117–142. [CrossRef]
79. Wang, B.; Clemens, S.C.; Liu, P. Contrasting the Indian and East Asian monsoons: Implications on geologic timescales. *Mar. Geol.* **2003**, *201*, 5–21. [CrossRef]
80. Yu, L.; Josey, S.A.; Bingham, F.M.; Lee, T. Intensification of the global water cycle and evidence from ocean salinity: A synthesis review. *Ann. N. Y. Acad. Sci. Spec. Issue Year Clim. Sci. Res.* **2020**, *1472*, 76–94. [CrossRef] [PubMed]